

A multiblob approach to colloidal hydrodynamics with inherent lubrication

Adolfo Vázquez-Quesada, Florencio Balboa Usabiaga
*Departamento de Física Teórica de la Materia Condensada,
Universidad Autónoma de Madrid, 28049 Madrid, Spain.*

Rafael Delgado-Buscalioni
*Departamento de Física Teórica de la Materia Condensada, Universidad Autónoma de Madrid,
and Institute for Condensed Matter Physics (IFIMAC). 28049 Madrid, Spain**

This work presents an intermediate resolution model of the hydrodynamics of colloidal particles based on a mixed Eulerian-Lagrangian formulation. The particle is constructed with a small set of overlapping Peskin's Immersed Boundary kernels (blobs) which are held together by springs to build up a particle impenetrable core. Here, we used 12 blobs placed in the vertexes of an icosahedron with an extra one in its center. Although the particle surface is not explicitly resolved, we show that the short-distance hydrodynamic responses (flow profiles, translational and rotational mobilities, lubrication, etc) agree with spherical colloids and provide consistent effective radii. A remarkable property of the present multiblob model is that it naturally presents a “divergent” lubrication force at finite inter-particle distance. This permits to resolve the large viscosity increase at dense colloidal volume fractions. The intermediate resolution model is able to recover highly non-trivial (many-body) hydrodynamics using *small particles* whose radii are similar to the grid size h (in the range $[1.6 - 3.2]h$). Considering that the cost of the embedding fluid phase scales like the cube of the particle radius, this result brings about a significant computational speed-up. Our code *Fluam* works in Graphics Processor Units (GPU's) and uses Fast Fourier Transform for the Poisson solver, which further improves its efficiency.

I. INTRODUCTION

The hydrodynamic interaction between colloidal molecules is a central problem in complex liquid physics which percolates over many disciplines and applied research: from low Reynolds hydrodynamics [1, 2] to turbulent particle laden flow [3, 4]. There is a solid theoretical corpus on hydrodynamic interactions in the low Reynolds limit [1, 5, 6] which over the years have derived most of the closed analytic forms for the friction and mutual mobilities between pairs of colloidal particles of different shapes as a function of their distance (see e.g. citations in Refs. [7, 8]). Colloidal hydrodynamics is however a many-body problem and many body effects become significant over a range of colloidal distances [1], which can even induce synchronization of many particles motion [9]. Computer simulation is a key tool to disentangle hydrodynamic effects on colloidal suspensions and in some sense it faces the same sort of difficulty or limitations encountered in analytically multipole expansions and multiple reflection methods [1, 10]. Hydrodynamic interactions between macromolecules crucially depend on the average separation between them and on the solute structure and physical properties (surface, permeability, elasticity, etc..). When dealing with soft and permeable molecules such as linear polymers in a dilute solution, it is enough to consider mobility relations based on pair-wise interactions which just include the lower order terms of the multipolar expansion, valid at large interparticle distances (compared with the polymer radius). The same approach is valid for dilute solution of rigid colloids, however, when in more concentrated solution of volume fraction typically above about 15%, higher order terms in their hydrodynamic interactions start to become relevant. At dense concentrations (above 30% in volume) the average distance between particles is a fraction of the particle radius and lubrication forces have to be resolved. Lubrication is undoubtedly the most difficult issue for any numerical solver because it is a friction force which diverges at zero particle distance. Physically it arises from the pressure needed to squeeze the fluid between two very near particles, so in principle, the numerical solver needs to be able to resolve the fluid motion between the particles up to very small scales, well below the particle size. The hard way to solve this dilemma is to increase the resolution of the fluid numerical solver around the particle and of the particle surfaces themselves or using accurate and expensive techniques, such as the spectral boundary

*Electronic address: rafael.delgado@uam.es

method [11]. However, due to the divergent nature of lubrication forces, computer power soon limits the resolution and the number of colloids and the accessible time window of the study.

Resolving lubrication forces by explicitly solving the fluid motion across tiny regions between the colloids is a difficult and costly route for any numerical scheme. In fact, it is even an impossible one if the fluid-particle coupling is based on the Stokes frictional coupling ansatz [12], because in this case only the lower order terms of the hydrodynamic multipolar expansion (large interparticle distances) will be correctly captured. In these Stokes-coupling schemes a clever strategy to by-pass this bottleneck has been to introduce the theoretical lubrication force provided by lubrication theory, *ad hoc* into the scheme for particle interactions [7, 12]. This “patched” lubrication does not arise from the motion of the fluid phase, but surely ensures that the friction between particle *pairs* corresponds to the theoretical expectation. Three body effects are neglected, although the role of many body interactions are screened in very dense suspensions and probably lessens [8]. In fact, the idea has been successful in dense solutions of colloidal spheres [8]. Extending this method to more complex molecules is, however, not straightforward. Implementation on non-spherical geometries requires having theory and analytic expressions beforehand. To further complicate things, it demands some far-from-trivial code adaptations, such as for instance, an (iterative) search of the nearest points between two objects and the determination of tangent planes: the reader is referred to Ref. [7] for an interesting recent work in that direction. Another issue to consider is that lubrication manifests in quite different forms depending on the relative motion of the objects (normal or tangential relative motion) and also on the type of boundary conditions at the surface (bubbles, drops, slip on rigid surfaces, etc). Finally, lubrication also involves translation-rotation coupling which cannot be ignored in many scenarios [6].

Despite the inherent difficulties, direct numerical simulations (DNS) of lubrication, based on the resolution of the underlying fluid motion around the colloids, certainly targets a more flexible and general scheme. This route obviously requires the imposition of the proper boundary conditions at the colloid surface: the most common no-slip surface, and generalizations allowing for fluid slip in several ways, depending on the particular method and particle type considered [13, 14]. The computational cost of mutual friction and eventually lubrication largely depends on the scheme used. Particle based methods, such as Smooth Particle Hydrodynamics (SPH) or Stochastic Rotation Dynamics (SRD) [15] are not adapted to resolve friction at short distances and require large resolution in terms of numbers of solvent particles per unit volume to correctly reproduce lubrication forces. Indeed, preliminary benchmark simulations comparing colloidal lubrication with SPH with our Eulerian solver with the Immersed Boundary Method, show that SPH requires much more computational resources to resolve squeezing flow. Again, a possible solution is to separately deal with lubrication by introducing *ad hoc* theoretical corrections to pairwise friction forces; this idea has been recently implemented in splitting integration schemes for spherical SPH particles [16] and also in Stokesian Dynamics, using the so called Fast Lubrication Method [8] for spheroids.

Direct numerical simulation of lubrication using Eulerian solvers (where the fluid motion is resolved in a grid using finite volume, finite differences or the Lattice Boltzmann method) need to resolve the particle surface where to impose the desired boundary condition, which in practice involves modifying the flow over the nearby fluid sites. There are several possible strategies. Lattice Boltzmann solvers have the possibility of defining collision rules for the border-sites between the solid and the fluid which modify the underlying “microscopic” LB distribution function in the advection step [12] in ways that might represent no-slip or slip surfaces. Works using this method use particle diameters between 10 and 40 fluid cells (or lattices) to patch the lubrication correction at colloidal separations below 5% of the particle radius [17]. Similar diameters are reported in previous works using finite elements [1], Direct Forcing [18–20], the Smooth Profile method [21]

Immersed Boundary method [22] is another referential method which has many variants such as the Direct Forcing method [18, 20] or the Stochastic Immersed Boundary method [23]. Direct Forcing, uses marker points over the particle *surface* where to impose the no-slip condition. Surface or boundary conditions are converted into volume forces which are spread over the fluid cells inside the local kernel to ensure zero relative fluid-particle velocity in it. In this work we carry out a similar strategy with an important difference: our resolution target is not the particle surface. From previous works we know that the “physical” volume of each blob and its hydrodynamic size (which is about one mesh size h) is determined by its kernel [24, 25]. The idea of a multi-blob particle formed by overlapping blob-kernels, is then not to resolve any surface, but to let the surface (or more properly, the particle size and shape) emerge from the reconstruction of the particle body. This subtlety is important because our goal is to develop an intermediate level of particle resolution, where colloids are of the same size of the mesh (the smallest radius hereby considered is $R \simeq 1.5h$) but still present an impenetrable core and significant

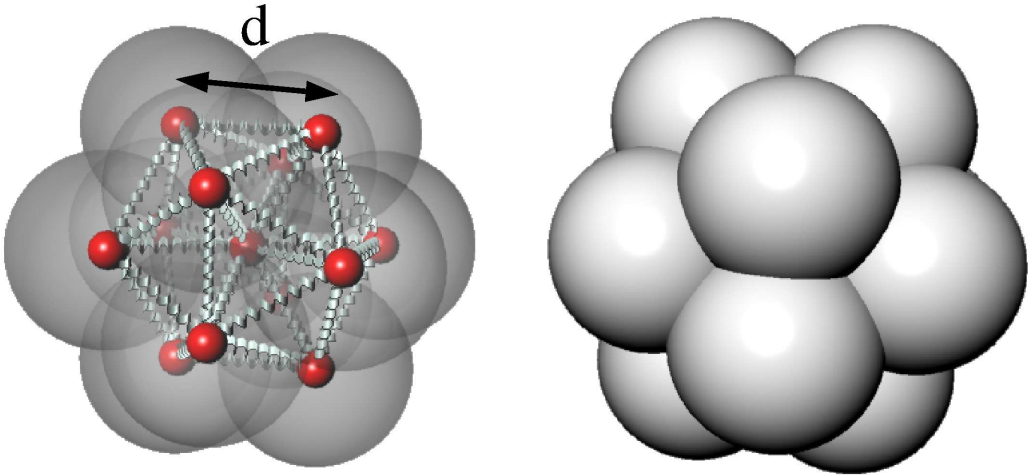


FIG. 1: A multiblob particle formed by $N = 13$ blobs placed in the 12 vertex of an icosahedron and its center. The size of the particle is determined by the distance between vertex, d . Blobs centers (red balls in the figure) are held together by hard springs, as indicated in the figure.

lubrication forces. Lubrication forces arise “naturally” from the fluid solver and quite importantly, *increase without bounds at finite inter-particle distances*. This “divergence” of the model’s lubrication comes out from a nice property of single blob kernels, whose mutual friction diverge at full overlap [24, 26]. This result opens the possibility of studying lubrication effects using rather small particles whose radius is about $1.5h$. It has to be stressed that for fixed accuracy in the mutual mobility resolution, a linear reduction in the particle size permits a cubic reduction in the fluid volume, which is certainly substantial and permits longer simulations with more particles. On a broader perspective, it also offers another route to lubrication of complex shapes.

In this work the blob forming the multiblob particles are held together using hard harmonic springs. This is certainly not an efficient method if one is interested in rigid body *motion* and alternatives have been already proposed [20, 21, 27] and implemented in schemes with linear accuracy in the time stepping. However, the stresslets arising from the rigid body *constraint* are more difficult to implement and probably require iterative schemes; in the present approach the contribution from the particle stress is provided by the connecting internal springs. The choice of the model connectivity is in part practical, as one of our next research goals is elasticity effects in colloid hydrodynamics which despite its relevance in many disciplines (notably in biology, microgels and even in nano-clusters) has been seldom considered in the literature (see the recent paper by Felderhof [28]). We recently developed single blob models with arbitrary compressibility [29] and the elastic multiblob naturally generalize to particles with arbitrary Young modulus.

We will first present in Sec. II the multiblob model which in this work has the icosahedron shape. This platonic solid hugs its inscribed sphere the most tightly and its surface area to volume ratio is the closest to a sphere of the same volume. Using the smallest icosahedron tessellation, with 12 vertexes one gets a volume filling factor (ratio between the icosahedron and sphere volume) of $\simeq 0.61$. In Section III discuss the hydrodynamic properties and induced stress of one multiblob from the analysis its equation of motion. Then in Sec. IV we use this analysis to derive the particle volume and mass, and momentum of inertia. The model hydrodynamic behavior starts with a study of its Stokeslet and rotlet response at long distances (Sec. V), proving consistency with Einstein relation (between the hydrodynamic radius and self-diffusion). We then focus on the particle hydrodynamics at closer distances, and study the flow velocity profile past the multiblob, Sec. VII. Pair hydrodynamic interactions (normal and tangential mobilities, translation-rotation coupling and lubrication curves) are studied in Sec. VIII. To conclude the tests in Sec. IX we study the effective viscosity of an ensemble of multiblobs and observe an excellent agreement with Batchelor’s celebrate result for spheres. We also show that the model can reproduce the viscosity increase at larger volume fractions. We conclude with comments on the model consistency and the sort of methodological research this study suggest taking for further improvements.

II. MULTIBLOB PARTICLE MODEL

The multiblob particle consists on a set of N linked blobs to form a bigger particle. In this work the blobs are linked with hard springs to conform an icosahedron, as shown in Fig. 1. In order to investigate the effect of possible leakage of fluid into the particle domain on its hydrodynamic properties (mutual friction, lubrication) we have considered two models: an icosahedron with $N = 12$ where blobs are placed at its vertexes and it is empty inside, and another model with an extra blob in the center to form a filled icosahedron with $N = 13$ blobs. The baricenter of the particle \mathbf{q}_0 is given by the positions of the blobs \mathbf{q}_i ,

$$\mathbf{q}_0 = \frac{1}{N} \sum_i \mathbf{q}_i \quad (1)$$

$$\mathbf{q}_i = \mathbf{q}_0 + \mathbf{s}_i \quad (2)$$

The translation velocity of the particle is

$$\mathbf{U}_0 = \frac{1}{N} \sum_{i=1}^N \mathbf{u}_i. \quad (3)$$

The particle motion has also degrees of freedom related to rotation and vibration of blobs around the baricenter. For any blob, the equilibrium distance s_i^{eq} to the icosahedron center is fixed by the spring. For the blobs in the shell, $s_i^{eq} = a$ where a is the icosahedron radius ($a \simeq 0.950 d$ in terms of inter-vertex distance d). In this work the springs are hard enough to neglect vibration or fluctuations around the equilibrium sites, i.e. $s_i \simeq s_i^{eq}$. In this rigid body limit we can write,

$$\mathbf{u}_i = \mathbf{U}_0 + \boldsymbol{\Omega} \times \mathbf{s}_i, \quad (4)$$

We apply the *no-slip* condition to each blob, so the fluid velocity $\mathbf{v}(\mathbf{r})$ in the blob domains follows the particle. In the continuum formulation the *no-slip* condition corresponds to [24, 26]

$$\mathbf{u}_i = \mathbf{J}_i \mathbf{v} = \int \delta_h(\mathbf{r} - \mathbf{q}_i) \mathbf{v}(\mathbf{r}) d\mathbf{r} \quad (5)$$

where \mathbf{J}_i is the interpolator operator of blob- i and $\delta_h(\mathbf{r} - \mathbf{q}_i)$ is the blob kernel, here constructed as a tensorial product of the 3-point Peskin's function $\Phi(x)$ [22, 26, 30],

$$\delta_h(\mathbf{r}) = h^{-3} \prod_{\alpha=1}^3 \Phi \left[\frac{r_\alpha}{h} \right] \quad (6)$$

with h the regular mesh size used in the present method. In the discrete setting, the integral in Eq. (5) is converted into a sum over all the lattice cells. The interpolator δ_h inherits all the grid-independence features of the 3-point Peskin's function $\Phi(x)$. In particular: the zeroth and first moments and the discrete L^2 -norm of the kernel are grid independent. The two first conditions are $\int \delta_h(\mathbf{r} - \mathbf{q}) \mathbf{r}_\alpha^n d\mathbf{r}^3 = q_\alpha^n$ for $n = 0$ and $n = 1$, while the last condition means that $\int \delta_h(\mathbf{r})^2 d\mathbf{r}^3 = \mathbb{V}^{-1}$, where for a blob particle model in a compressible fluid [26, 29], $\mathbb{V} = 8 h^3$ is the volume of fluid occupied by the particle.

We introduce the multiblob interpolator \mathcal{J} ,

$$\mathcal{J} \equiv \frac{1}{N} \sum_i \mathbf{J}_i \quad (7)$$

which provides the translation multiblob velocity from the underlying fluid velocity field,

$$\mathbf{U}_0 = \mathcal{J} \mathbf{v}. \quad (8)$$

The adjoint of the blob interpolator \mathbf{J}_i is the spreading operator which distributes the force \mathbf{F}_i acting on each blob as a force density to the fluid phase, $\mathbf{f}_i(\mathbf{r}) = \mathbf{S}_i \mathbf{F}_i = \delta_h(\mathbf{r} - \mathbf{q}_i) \mathbf{F}_i$ (see [24, 25]). As before one can introduce the overall spreading operator

$$\mathbf{S} \equiv \frac{1}{N} \sum_i \mathbf{S}_i = \frac{1}{N} \sum_i \delta_h(\mathbf{r} - \mathbf{q}_i) \quad (9)$$

which transmits *net* forces on the multiblob particle to the surrounding fluid.

As stated, the average and spreading operators of the isolated blob are adjoint and ensure certain important properties [24]: Grid independence of the zeroth and first moments $\mathbf{J}_i[1] = 1$ and $\mathbf{J}_i[\mathbf{r} - \mathbf{q}_i] = 0$ and constant norm, which can be generally expressed as $\mathbf{J}_i \mathbf{P} \mathbf{S}_i = \mathbf{V}^{-1}$, where in the compressible setting $\mathbf{P}^{\alpha, \beta} = \delta_{\alpha, \beta}$ is just the identity operator while, in the incompressible limit, \mathbf{P} is the solenoidal projector which applied to a vector field, provides its divergence-free component (see Ref. [24]). For $\mathbf{P} = \mathbf{1}$ (compressible case) the inverse volume matrix is independent on the grid and $\mathbf{V}^{-1} = \mathbb{V}^{-1} \mathbf{1}$. In this incompressible setting, due to the instantaneous elimination of the sound modes [24, 25], the effective particle volume is slightly larger, $\tilde{\mathbb{V}} = (3/2)\mathbb{V}$, consistently with the added mass effect of a real particle in an incompressible fluid [31, 32]. In the incompressible discrete formulation [24, 25] we observe that $\mathbf{V}^{-1} \approx \tilde{\mathbb{V}}^{-1} \mathbf{1}$ (about 1% deviation). Following with the blob-multiblob equivalence, due to the linearity of \mathcal{J} and \mathcal{S} , it is easy to see that \mathcal{J} and \mathcal{S} are also adjoint and have grid independent zeroth and first moments, $\mathcal{J}[1] = 1$ and $\mathcal{J}[\mathbf{r} - \mathbf{q}_0] = 0$ (where \mathbf{q}_0 is the geometric center of the multiblob). As an extrapolation of the equivalences with the single blob case analyzed in Ref. [24, 25], the operator,

$$\mathcal{J} \mathbf{P} \mathcal{S} = \frac{\sum_{i,j} \mathbf{J}_i \mathbf{P} \mathcal{S}_j}{N^2} \quad (10)$$

should ideally be proportional to the inverse of the multiblob volume, $\tilde{\mathbb{V}}_m$. Moreover, we show in subsequent sections that, for our isotropic body this operator present small deviations from a scalar, i.e., $\mathcal{J} \mathbf{P} \mathcal{S} \simeq (\tilde{\mathbb{V}}_m)^{-1} \mathbf{1}$.

III. MULTIBLOB DYNAMICS

The particle we consider in this work is not completely rigid. It is formed by blobs connected by hard springs so formally it corresponds to the type of flexible structures treated in immersed boundary methods [22]. The interblob springs are however stiff enough to ensure that the amplitude of particle vibrations are small which in practice, it means that the frequency of the springs is faster than the rate of viscous fluid momentum distribution around the particle. Using springs to connect the blobs and form multiblobs permits us to use the same solvers we have recently developed for single blob dynamics in different hydrodynamic regimes [25]. For this work we have mainly used the Inertial Coupling method for particles in incompressible fluid [24] (which includes both fluid and particle inertia) and also the Fluctuating Immersed Boundary method [33], adapted to the Stokesian limit, where the particle and fluid inertia is absent. In this section we discuss the hydrodynamic response and properties of one multiblob, arising from their equations of motion.

A. Translational motion

The velocity of one blob i in the particle can be decomposed in the particle translation velocity \mathbf{U}_0 and a peculiar velocity \mathbf{u}'_i ,

$$\mathbf{u}_i = \mathbf{U}_0 + \mathbf{u}'_i, \quad (11)$$

Neglecting the small vibrations of the blobs, the instantaneous angular velocity $\boldsymbol{\Omega}$ of the body can be determined from $\mathbf{u}'_i = \boldsymbol{\Omega} \times \mathbf{s}_i$, which is an exact relation for a rigid body.

In our model the incompressible fluid velocity field with a single multiblob particle evolves according to,

$$\rho_f \frac{\partial \mathbf{v}}{\partial t} = -\nabla \pi - \nabla \cdot \boldsymbol{\sigma}_f - \sum_j \mathbf{S}_j \boldsymbol{\lambda}_j = \mathbf{P} \left(\nabla \cdot \boldsymbol{\sigma}_f - \sum_j \mathbf{S}_j \boldsymbol{\lambda}_j \right) \quad (12)$$

where π is the hydrodynamic pressure or the Lagrangian multiplier ensuring the incompressibility condition $\nabla \cdot \mathbf{v} = 0$ and $\boldsymbol{\sigma}_f = -\eta \mathbf{E} + \tilde{\boldsymbol{\sigma}} + \rho_f \mathbf{v} \mathbf{v}$ contains the viscous stress constructed with the symmetric part of the fluid strain ($\mathbf{E} \equiv (\nabla \mathbf{v} + \nabla \mathbf{v}^T)/2$) and the convective inertia, given by the dyadic $\rho_f \mathbf{v} \mathbf{v}$. Hydrodynamic fluctuations (either in compressible or incompressible flow) can be also included via a

fluctuating stress $\tilde{\boldsymbol{\sigma}}$ as explained in Refs. [24, 26], whose validity is restricted to small departures from the equilibrium state (Gaussian statistics).

The LHS of the momentum density equation can be also formally written without the hydrodynamic pressure π using the operator \mathbf{P} which projects any field on its solenoidal sub-space $\nabla \cdot \mathbf{P}\mathbf{v} = 0$.

The force $\boldsymbol{\lambda}_i$ is a Lagrangian multiplier ensuring the *no-slip* condition on each blob,

$$\mathbf{u}_i = \mathbf{J}(\mathbf{q}_i)\mathbf{v} = \mathbf{J}_i\mathbf{v}. \quad (13)$$

The fluid-particle force $\boldsymbol{\lambda}_i$ is also present in the blob equation of motion (see Ref. [25]),

$$\boldsymbol{\lambda}_i = m_{e,i}\dot{\mathbf{u}}_i - \mathbf{f}_i, \quad (14)$$

where $m_{e,i}$ is its excess mass and the total mass of the *isolated* blob is

$$m_i = \rho_f \tilde{\mathcal{V}} + m_{e,i}. \quad (15)$$

The blob equation of motion can be also obtained by noting that

$$\frac{d\mathbf{u}_i}{dt} = \mathbf{J}_i \left(\frac{\partial \mathbf{v}}{\partial t} \right) + \mathbf{a}_i \quad (16)$$

where $\mathbf{a}_i \equiv \mathbf{u}_i \cdot \nabla_{\mathbf{q}} \mathbf{J}_i \mathbf{v}$ is the convective acceleration arising from the material derivative relative to the blob translation (see [24, 29]).

Applying \mathbf{J}_i in Eq. (12) leads to,

$$\rho_f \dot{\mathbf{u}}_i = - \sum_j \mathbf{J}_i \mathbf{P} \mathbf{S}_j \boldsymbol{\lambda}_j - \mathbf{J}_i \mathbf{P} \nabla \cdot \boldsymbol{\sigma}_f + \rho_f \mathbf{a}_i \quad (17)$$

Introducing Eq. (14) and the density matrix operator,

$$\boldsymbol{\rho}_{i,j} \equiv \rho_f \delta_{ij} + \mathbf{J}_i \mathbf{P} \mathbf{S}_j m_{e,j}$$

Eq. (17) can be expressed explicitly in terms of the set of blob accelerations,

$$\sum_j \boldsymbol{\rho}_{i,j} \dot{\mathbf{u}}_j = \sum_j \mathbf{J}_i \mathbf{P} \mathbf{S}_j \mathbf{f}_j - \mathbf{J}_i \mathbf{P} \nabla \cdot \boldsymbol{\sigma}_f + \rho_f \mathbf{a}_i. \quad (18)$$

The forces acting on each blob can be decomposed in a net contribution to the particle translation and peculiar components, i.e.

$$\boldsymbol{\lambda}_i = \frac{1}{N} \boldsymbol{\Lambda}_0 + \boldsymbol{\lambda}'_i, \quad (19)$$

$$\boldsymbol{\Lambda}_0 = \sum_i m_{e,i} \dot{\mathbf{u}}_i - \mathbf{F}_0, \quad (20)$$

$$\mathbf{f}_i = \frac{1}{N} \mathbf{F}_0 + \mathbf{f}'_i. \quad (21)$$

The total non-hydrodynamic force acting on the particle is \mathbf{F}_0 and the peculiar force \mathbf{F}'_i sums to zero ($\sum_i \mathbf{f}'_i = 0$) and contains contributions from external torque and internal force (springs). The fluid contributes with a net $\boldsymbol{\Lambda}_0$ force on the multiblob, which equals $-\mathbf{F}_0$ if the particle has no inertia ($m_{e,i} = 0$ for each blob).

The equation of motion of the multiblob geometric center $\mathbf{q}_0 = (1/N) \sum_i \mathbf{q}_i$ is obtained by summing over the N blobs in Eq. (17). If all the excess masses are similar $m_{e,i} = m_e$ the motion of the geometric and the center of mass coincide and its acceleration $\dot{\mathbf{U}}_0$ is given by,

$$\rho_m \dot{\mathbf{U}}_0 = \mathcal{J} \mathbf{P} \mathbf{S} \mathbf{F}_0 - \mathcal{J} \mathbf{P} \left[\nabla \cdot \boldsymbol{\sigma}_f + \sum_j \mathbf{S}_j \boldsymbol{\lambda}'_j \right] + \rho_f \mathbf{a}_0. \quad (22)$$

where we have defined the average multiblob density as,

$$\rho_m = \rho_f \mathbf{1} + N \mathcal{J} \mathbf{P} \mathbf{S} m_e = \frac{1}{N} \sum_{i,j} \boldsymbol{\rho}_{i,j} \quad (23)$$

Equation (22) reflects that the particle translation velocity is not only affected by the net force but also by the distribution of peculiar blob forces. Physically this is related to the translation-rotation coupling [6] or in the case of elastic particles translation-vibration coupling [28], much less studied in the literature. In an isotropic body \mathcal{JPS} should be a scalar [6], however deviations might occur in the discrete setup leading to spurious forces. We will come back to this issue later.

B. Rotational motion

The equation of motion for the multiblob angular velocity $\boldsymbol{\Omega}$ can be derived from Eq. (18), by performing the vector product $\mathbf{s}_i \times$ summing over the blobs of the multiblob. In the most general case (a multiblob with arbitrary excess mass distribution $m_{e,i}$),

$$\sum_{i,j} \mathbf{s}_i \times \boldsymbol{\rho}_{i,j} \dot{\mathbf{u}}_i = \sum_j \mathbf{s}_i \times \mathbf{J}_i \mathbf{P} \mathbf{S}_j \mathbf{f}_j - \sum_i \mathbf{s}_i \times \mathbf{J}_i \mathbf{P} \nabla \cdot \boldsymbol{\sigma}_f + \rho_f \sum_i \mathbf{s}_i \times \mathbf{a}_i \quad (24)$$

This equation contains a significant amount of well known hydro-mechanical couplings: such as crossed inertial terms which might induce rotation from translational accelerations, torques arising from non-homogeneous mass distributions and also in the Stokes limit, crossed rotational-translational mobilities. In the present work we shall just focus on the inertia-less, neutrally buoyant case ($m_{e,i} = 0$ and $\boldsymbol{\rho}_{i,j} = \rho_f \delta_{i,j}$) and will consider isotropic bodies, where the translation-rotational mobility coupling is absent. Consider a pure rotational motion of the icosahedron induced by an external torque resulting from a set of forces on the blobs given by $\mathbf{f}_i = \boldsymbol{\alpha} \times \mathbf{s}_i$, where $\boldsymbol{\alpha}$ is a constant vector. The resulting torque is,

$$\boldsymbol{\tau} = \sum_i \mathbf{s}_i \times \mathbf{f}_i = \sum_i \mathbf{s}_i \times \boldsymbol{\alpha} \times \mathbf{s}_i = \mathbb{I}_0 \boldsymbol{\alpha} \quad (25)$$

where we have defined the tensor,

$$\mathbb{I}_0 = \sum_i [s_i^2 \mathbf{1} - \mathbf{s}_i \mathbf{s}_i] \quad (26)$$

Applying the time derivative to $\mathbf{u}_i = \mathbf{U}_0 + \boldsymbol{\Omega} \times \mathbf{s}_i$ and using that $\mathbf{f}_i = \boldsymbol{\alpha} \times \mathbf{s}_i$, one gets, after some manipulations in Eq. (24),

$$\rho_f \left[\mathbb{I}_0 \dot{\boldsymbol{\Omega}} + \sum_{i,j} \mathbf{s}_i \times (\boldsymbol{\Omega} \times (\boldsymbol{\Omega} \times \mathbf{s}_j)) \right] = \mathbb{I}_c \mathbb{I}_0^{-1} \boldsymbol{\tau} - \sum_i \mathbf{s}_i \times \mathbf{J}_i \mathbf{P} \nabla \cdot \boldsymbol{\sigma}_f + \rho_f \sum_i \mathbf{s}_i \times \mathbf{a}_i, \quad (27)$$

The torque arising from the convective force $\sum_i \mathbf{s}_i \times \mathbf{a}_i$ can only be significant at large particle Reynolds number, which shall not be considered in this work. The term $\sum_{i,j} \rho_f \mathbf{s}_i \times (\boldsymbol{\Omega} \times (\boldsymbol{\Omega} \times \mathbf{s}_j))$ vanishes for isotropic homogeneous bodies and shall not be considered hereafter. To obtain the first term on the RHS of Eq. 27, $\mathbb{I}_c \mathbb{I}_0^{-1} \boldsymbol{\tau}$ we have write it as $\sum_{i,j} \mathbf{s}_i \times (\mathbf{J}_i \mathbf{P} \mathbf{S}_j (\boldsymbol{\alpha} \times \mathbf{s}_j)) = \mathbb{I}_c \boldsymbol{\alpha}$ (see below) and then introduced the relation for the external torque $\boldsymbol{\alpha} = \mathbb{I}_0^{-1} \boldsymbol{\tau}$. Using the above assumptions, Equation (24) becomes,

$$\rho_f \mathbb{I}_0 \dot{\boldsymbol{\Omega}} = \mathbb{I}_c \mathbb{I}_0^{-1} \boldsymbol{\tau} - \sum_i \mathbf{s}_i \times \mathbf{J}_i \mathbf{P} \nabla \cdot \boldsymbol{\sigma}_f. \quad (28)$$

The second order tensor \mathbb{I}_c can be expressed in terms of the Levi-Civita third order tensor $\epsilon^{\alpha,\beta,\gamma}$ used in cross-product manipulations (note that Einstein convention is used for superindexes which corresponds to spatial directions, while subindexes to the blobs)

$$\mathbb{I}_c^{\alpha,\mu} \equiv \sum_{i,j} \epsilon^{\alpha,\beta,\gamma} \epsilon^{\lambda,\mu,\nu} s_i^\beta s_j^\nu (\mathbf{J}_i \mathbf{P} \mathbf{S}_j)^{\gamma,\lambda} \quad (29)$$

which can be further re-expressed using operations with second order tensors [34]. In the incompressible fluid case \mathbb{I}_c is difficult to calculate because the tensorial character of $\mathbf{J}_i \mathbf{P} \mathbf{S}_j$ modifies the direction of

any vector which is applied to. The compressible case ($\mathbf{P} = \mathbf{1}$) is simpler because $\mathbf{J}_i \mathbf{S}_j$ is a scalar so $\mathbf{s}_i \times (\mathbf{J}_i \mathbf{S}_j (\boldsymbol{\alpha} \times \mathbf{s}_j)) = \mathbf{J}_i \mathbf{S}_j (\mathbf{s}_i \times (\boldsymbol{\alpha} \times \mathbf{s}_j))$ and,

$$\mathbb{I}_c = \sum_{i,j} \mathbf{J}_i \mathbf{S}_j [\mathbf{s}_i \cdot \mathbf{s}_j \mathbf{1} - \mathbf{s}_j \mathbf{s}_i]. \quad (30)$$

$$(31)$$

We finally note that $\dot{\mathbf{L}} = \rho_f \mathbb{I}_0 \dot{\boldsymbol{\Omega}}$ is just the time derivative of the angular momentum density of the (neutrally buoyant) particle

$$\mathbf{L} = \rho_f \sum_i \mathbf{s}_i \times \mathbf{u}_i. \quad (32)$$

Equation (27) or (28) permits to evaluate the multiblob momentum of inertia, which will be presented in Sec. IV along with an alternative derivation based on the equipartition theorem.

C. Stresslet

Unlike the single blob particle model, the multiblob is able to create stress on the fluid due to its cohesive forces. This can clearly be observed by expressing the particle force density contribution to the fluid momentum equation 12 in the form of the divergence of a particle pressure tensor. To that end we expand the spreading function of a single blob in a Taylor series around $\mathbf{r} - \mathbf{q}_0$,

$$\mathbf{S}(\mathbf{r} - \mathbf{q}_i) = \mathbf{S}(\mathbf{r} - \mathbf{q}_0 - \mathbf{s}_i) = \mathbf{S}(\mathbf{r} - \mathbf{q}_0) - \nabla_{\mathbf{r}} \mathbf{S}(\mathbf{r} - \mathbf{q}_0) \cdot \mathbf{s}_i + \text{h.o.t.} \quad (33)$$

So the particle contribution in Eq. 12 becomes,

$$-\sum_i \mathbf{S}(\mathbf{r} - \mathbf{q}_i) \boldsymbol{\lambda}_i = -\mathbf{S}(\mathbf{r} - \mathbf{q}_0) \boldsymbol{\Lambda}_0 + \nabla_{\mathbf{r}} \cdot \left[\mathbf{S}(\mathbf{r} - \mathbf{q}_0) \sum_{i=1}^N \mathbf{s}_i \boldsymbol{\lambda}'_i \right] + \text{h.o.t.} \quad (34)$$

The first term in Eq. (34) is the monopole contribution of the multiblob particle (net force) while the dipolar contribution only involves peculiar (fluid-particle) forces $\boldsymbol{\lambda}'$ (as $\sum_i \mathbf{s}_i = 0$). Higher order terms in the expansion (34) become relevant if the particle size is comparable with the smallest wavelength $2\pi/k$ of the fluid velocity spectra. This can be seen by performing a Fourier transform (in \mathbf{r}) over the full expansion of Eq. 34 and realizing that the next term in the pressure tensor is proportional to $(i/2)\mathbf{k}\mathbf{s}$. In most colloidal applications, the characteristic length of the flow is much larger than the colloidal size, $ka \ll 1$ (we were not able to find a study on the effect of higher order multipoles in the viscosity of colloidal fluids). The dipole term in Eq. (34), whose dyadic is usually decomposed in a rotational (skew-symmetric part) and a stresslet (zero trace, symmetric part) [1], takes now the form $-\nabla \cdot \boldsymbol{\sigma}_p$ where the components of particle pressure tensor are,

$$\sigma_p^{\alpha,\beta} = -\mathbf{S}(\mathbf{r} - \mathbf{q}_0) \sum_{i=1}^N \langle s_i^\alpha \mathbf{f}_i^{\prime\beta} \rangle \quad (35)$$

Where we have assumed a case where inertia is negligible so that $\boldsymbol{\lambda}_i = -\mathbf{f}_i$ (see Eq. 14). The average is made over the fast dynamics of the multiblob, which depending on the application (or relevant time scale) might include the vibrational modes only, or the translational and rotational degrees of freedom as well. The contribution of one particle to the pressure tensor is thus sustained by its internal virial term.

Equation (35) shows that the dipolar contribution of the multiblob model is the sum of N dipoles $\mathbf{s}_i \mathbf{f}_i$. In the present model the position of the blob i with respect of the body center \mathbf{q}_0 can fluctuate $\mathbf{s}_i = \mathbf{a}_i + \delta \mathbf{s}_i$, (with $\mathbf{a}_i = a \mathbf{n}_i$ the radius vector to embedding sphere). Thus, the particle virial contain a rigid body contribution $\mathbf{a}_i \mathbf{f}_i$ and an elastic one $\delta \mathbf{s}_i \mathbf{f}_i$. The relevance of fluctuations of the body shape is determined by the ratio $\delta s_i/a$. Here, the displacement from the equilibrium position is $\delta s_i \sim f_i/k_{sp}$. In a fluid at rest, the equipartition of the spring energy in equilibrium establishes that $\delta s_i \sim (k_B T/k_{sp})^{1/2}$ and the ratio $\delta s_i/a \sim O(k_B T/k_{sp} a^2)^{1/2}$. Under straining motion $f_i \simeq 6\pi\eta E a^2$ (where E is the shear

rate) and in terms of the Peclet number $Pe = 6\pi\eta Ea^3/k_B T$ the relevance of the shape fluctuations scales like $\delta s_i/a \sim Pe(k_B T/k_{sp}a^2)$. In the present simulations we have used very stiff springs which ensure these non-dimensional groups are negligible small.

The stress released by the particle is directly related to the local stress of the fluid. For an inertia-less and force-free particle in straining fluid motion, the force on the blob i is the local surface traction of the fluid $\mathbf{f}'_i = (\pi\mathbf{1} + \boldsymbol{\sigma}_f) \cdot \mathbf{n}_i dA_i$ where dA_i is the surface element of the blob and $\mathbf{n}_i = \mathbf{s}_i/s_i$ is the surface vector. In the continuum limit of the body space coordinates, such relation would provide the proper continuum version of the particle stress, $\boldsymbol{\sigma}_p = \oint \mathbf{s}(\pi\mathbf{1} + \boldsymbol{\sigma}_f) \cdot \mathbf{n} dA$ [1]. It is possible to map our discrete formulation to the continuum formulae, however in this work we will analyze the consistency of the multiblob stresslet by considering its most prominent effect in the flow, which is the increase of the effective viscosity of a multiblob colloid suspension (see Sec. III C).

IV. MULTIBLOB VOLUME, MASS AND MOMENT OF INERTIA

In this section we use the relations obtained in Sec. III to derive several properties of the multiblob, such as its mass and moment of inertia. By ascribing the moment of inertia of the multiblob to that of a sphere (which in fact coincides with that of a solid icosahedron) we will obtain a first measure of the multiblob radius. To derive the mass and moment of inertia of the multiblob particle we analyze its inertia, from the transient of Eq. (22) and (28). Then, we show that the *inertial* evaluations are consistent with the *thermal* ones based on the equipartition of the translational and rotational kinetic energy.

A. Multiblob mass and volume

1. From the particle inertia

The inertial mass in Eq. (22) can be obtained by considering a particle pulled with a constant force \mathbf{F}_0 which is equally distributed over the forming blobs $\mathbf{f}_i = \mathbf{F}_0/N$. If the fluid is ideal $\mathbf{P}\nabla \cdot \boldsymbol{\sigma}_f = 0$ and initially at rest $\mathbf{a}_0 = 0$ in Eq. 22, the particle mass could be directly obtained from the ratio $M = F_0/\dot{U}_0$. In practice one can reproduce this situation by considering very short times $t \rightarrow 0$ after the force imposition, i.e., when the fluid still behaves like ideal, well before the onset of the frictional regime. In the Eulerian (inviscid) limit, the force $\mathcal{JPS}\mathbf{F}_0$ depends on the body shape, which can induce lift forces (normal to \mathbf{F}_0). However the lift is zero for (non-rotating) isotropic bodies. According to Eq. 22, the mass of the multiblob is well defined if the \mathcal{JPS} operator is proportional to the inverse of the particle volume so for our isotropic body we expect,

$$\mathcal{JPS}\mathbf{F}_0 = \tilde{\mathbb{V}}_m^{-1}\mathbf{F}_0 \quad (36)$$

where $\tilde{\mathbb{V}}_m$ is the multiblob volume. The situation is then similar to the single blob case [24], for which the relation $\mathcal{J}_i\mathbf{PS}_i = \tilde{\mathbb{V}}^{-1}\mathbf{1}$ is exact in the continuum periodic setting. In the discrete formulation it presents deviations of about 1% over the grid positions and directions [25]. In the multiblob case we expect that the extensive overlap does not substantially alter this quasi-independence of the particle volume with the grid. In principle, the blob kernels used to build the multiblob are not constructed to ensure such grid-independence. This kind of optimization still being an open problem [35]. Albeit, we have found that a set of overlapping Peskin's 3pt-kernels leads to small variations in mass, volume and hydrodynamic size of the multiblob icosahedron, with relative deviations which can be even smaller than that of a single blob (see Figure 2b). The (isotropic) particle density operator in Eq. (23) is then also almost regular, $\boldsymbol{\rho}_m \approx \rho_m\mathbf{1}$, with

$$\rho_m \approx \left(\rho_f + \frac{Nm_e}{\tilde{\mathbb{V}}_m} \right).$$

and the inertial mass is then also a scalar,

$$M = \rho_m \tilde{\mathbb{V}}_m. \quad (37)$$

Before presenting the results for $\tilde{\mathbb{V}}_m$, in the following section we prove that the inertial mass, derived from Eq. 22 is consistent with that appearing in the equipartition of its translational kinetic energy.

2. Mass from equipartition

The equipartition theorem applied to the multiblob translational energy $\langle U_0^2 \rangle = k_B T / M_{\text{th}}$, provides an alternative route to its mass which we have called ‘‘thermal mass’’ M_{th} . In the following calculation for M_{th} we consider a neutrally buoyant particle in a fluid with density ρ_f , so that $\tilde{\mathbb{V}}_m = M_{\text{th}} / \rho_f$.

We start by quoting the equipartition of the fluid degree’s of freedom, which can be generally written as [25]

$$\langle v^\alpha(\mathbf{r})v^\beta(\mathbf{r}') \rangle = \frac{k_B T}{\rho_f} \mathbf{P}^{\alpha,\beta} \delta(\mathbf{r} - \mathbf{r}'), \quad (38)$$

where α and β are the components of the covariance (dyadic). Recall that in the compressible formulation $\mathbf{P}^{\alpha,\beta} = \delta_{\alpha,\beta}$, however, in the incompressible fluid, fluctuations along different directions are correlated (within the same cell). The particle translational velocity is,

$$\mathbf{U}_0 = \frac{1}{N} \sum_i^N \mathbf{J}_i \mathbf{v} = \mathcal{J} \mathbf{v} \quad (39)$$

Using the no-slip condition over each blob $\mathbf{u}_i = \mathbf{J}_i \mathbf{v} = \int \delta_h(\mathbf{r} - \mathbf{q}_i) \mathbf{v}(\mathbf{r}) d\mathbf{r}$ one gets,

$$\langle U_0^\alpha U_0^\beta \rangle = \frac{1}{N^2} \sum_{i,j} \int \delta_h(\mathbf{r} - \mathbf{q}_i) \langle v^\alpha(\mathbf{r})v^\beta(\mathbf{r}') \rangle \delta_h(\mathbf{r}' - \mathbf{q}_j) d\mathbf{r} d\mathbf{r}' \quad (40)$$

In this evaluation we are implicitly assuming that the particle translational degrees of freedom are much slower than the fluid velocity so terms involving $\{\mathbf{q}_i\}$ can be frozen in the fluid thermal average (as customarily done in colloids, due to the very large Schmidt number) Using also Eq. 38,

$$\begin{aligned} \langle U_0^\alpha U_0^\beta \rangle &= \frac{k_B T}{N^2 \rho_f} \sum_{i,j} \int \int \delta_h(\mathbf{r} - \mathbf{q}_i) \mathbf{P}^{\alpha,\beta} \delta(\mathbf{r} - \mathbf{r}') \delta_h(\mathbf{r}' - \mathbf{q}_j) d\mathbf{r} d\mathbf{r}' = \\ &= \frac{k_B T}{N^2 \rho_f} \sum_{i,j} \int \delta_h(\mathbf{r} - \mathbf{q}_i) \mathbf{P}^{\alpha,\beta} \delta_h(\mathbf{r} - \mathbf{q}_j) d\mathbf{r} = \frac{k_B T}{\rho_f} \frac{1}{N^2} \sum_{i,j} \mathbf{J}_i \mathbf{P}^{\alpha,\beta} \mathbf{S}_j = \\ &= \frac{k_B T}{\rho_f} \mathcal{J} \mathbf{P}^{\alpha,\beta} \mathcal{S} \end{aligned} \quad (41)$$

Thus the thermal mass of the multiblob coincides with its inertial mass matrix. In case of an isotropic body $\mathcal{J} \mathbf{P} \mathcal{S} = \tilde{\mathbb{V}}_m^{-1} \mathbf{1}$ so $M_{\text{th}} = \rho_f \tilde{\mathbb{V}}_m$ in agreement with Eq. 37. The equipartition of translational kinetic energy is recovered as,

$$\langle U_0^2 \rangle = \frac{k_B T}{M} \quad (42)$$

B. Inertia tensor

1. From rotational inertia

Equation (27) can be applied to multiblobs with arbitrary shape and mass distribution. It permits to derive the inertia tensor by evaluating the initial angular acceleration upon the application of a given torque $\boldsymbol{\tau}$ at $t = 0$. In particular, we consider a fluid at rest and a particle with $\boldsymbol{\Omega} = 0$, which upon application of $\boldsymbol{\tau}$ will increase its angular velocity according to $\dot{\boldsymbol{\Omega}} = \mathcal{I}^{-1} \boldsymbol{\tau}$. From Eq. (28), the resulting tensor of inertia of the neutrally buoyant particle is,

$$\mathcal{I} = \rho_f \mathbb{I}_0 \mathbb{I}_c^{-1} \mathbb{I}_0 \quad (43)$$

For isotropic bodies (like a sphere, the icosahedron or any Platonic solid) both \mathbb{I}_0 , \mathbb{I}_c and also \mathcal{I} are scalars in the continuum setup (diagonal matrices with three similar eigenvalues) Again, in the discrete setup, \mathcal{I} is an operator which generally depends on the grid coordinate and the rotation direction. We advance that in the discrete grid, deviations of the constant scalar ‘‘behavior’’ of \mathcal{I} were found to be small (about 1%) as observed with the particle volume.

2. From equipartition

The inertia tensor can be also obtained from the equipartition of the rotational energy. In the case of neutrally buoyant particles we use the angular momentum defined in Eq. 32 and evaluate its covariance. We first have $\mathbf{L} = \rho_f \mathbb{I}_0 \boldsymbol{\Omega}$ so,

$$\langle \mathbf{L} \mathbf{L}^* \rangle = \rho_f^2 \mathbb{I}_0 \langle \boldsymbol{\Omega} \boldsymbol{\Omega}^* \rangle \mathbb{I}_0^t, \quad (44)$$

and from the definition (32) one gets,

$$\langle \mathbf{L} \mathbf{L}^* \rangle = \rho_f^2 \left\langle \sum_{i,j} (\mathbf{s}_i \times \mathbf{J}_i \mathbf{v}) (\mathbf{s}_j \times \mathbf{v}^* \mathbf{S}_j) \right\rangle = k_B T \rho_f \mathbb{I}_c. \quad (45)$$

which can be shown by using using Levi Civita tensors for the cross-products, as in Eq. (29) and also that $\langle \mathbf{v}(\mathbf{r}) \mathbf{v}^*(\mathbf{r}') \rangle = (k_B T / \rho_f) \mathbf{P} \delta(\mathbf{r} - \mathbf{r}')$. Combining both results, one gets the consistent equipartition relation,

$$\langle \boldsymbol{\Omega} \boldsymbol{\Omega}^* \rangle = k_B T \boldsymbol{\mathcal{I}}^{-1} \quad (46)$$

Numerical and analytic results for $\boldsymbol{\mathcal{I}}$ are presented in the next section. We advance that numerical values of $\boldsymbol{\mathcal{I}}$ obtained from the inertial route (angular acceleration after an external torque) and from equipartition (using Eq. 46) agree within less than about 1% for any value of d considered.

C. Analytic and numerical evaluation of mass, inertia moment and rotation radius

1. Mass and volume

The mass of the multiblob can be also expressed as,

$$M = \rho_f \tilde{\mathbb{V}}_m + N m_e = \boldsymbol{\rho}_m \tilde{\mathbb{V}}_m = \frac{N \boldsymbol{\rho}_m \tilde{\mathbb{V}}}{1 + (N-1) \hat{\alpha}} \quad (47)$$

where the non-dimensional factor $\hat{\alpha}$ measures the average overlap per blob,

$$\hat{\alpha} = \frac{1}{N(N-1)} \sum_{i,j \neq i} \langle \mathbf{J}_i \mathbf{P} \mathbf{S}_j \rangle_{grid} \tilde{\mathbb{V}}, \quad (48)$$

and involves the average of $(\mathbf{J}_i \mathbf{P} \mathbf{S}_j \mathbf{e}) \cdot \mathbf{e}$ acting over all possible unit vectors \mathbf{e} and grid locations; we noted it as $\langle \dots \rangle_{grid}$. This overlap factor $\hat{\alpha}$ ranges from $\hat{\alpha} = 1$ (full overlap between blobs, or $d = 0h$) to $\hat{\alpha} = 0$ (no-overlap, taking place at large d). In the first case, the particle mass is equivalent to a single blob with excess mass $N m_e$ and density $\boldsymbol{\rho}_m = \rho_f + N m_e / \tilde{\mathbb{V}}$, while in the former, the particle density is equal to that of single blob with mass m_e . In principle, the zero overlap limit ($\mathbf{J}_i \mathbf{P} \mathbf{S}_j = 0$) is only reached in the compressible case ($\mathbf{P} = \mathbf{1}$) where $\mathbf{J}_i \mathbf{P} \mathbf{S}_j > 0$ and equals zero when the two blobs are at distance $d > 3h$ along one direction (using 3pt kernels). In the incompressible case the dependence of $\hat{\alpha}$ with the interblob separation d is not that trivial because \mathbf{P} could induce negative overlap contributions $\mathbf{J}_i \mathbf{P} \mathbf{S}_j < 0$. Yet, the ‘‘dynamic’’ mass of the multiblob in a 3D incompressible fluid should consistently contain the fluid added mass. In other words if $\boldsymbol{\rho}_m \mathbb{V}_m$ is the multiblob mass in the compressible $\mathbf{P} = 1$ case; in the incompressible fluid it should be $(3/2) \boldsymbol{\rho}_m \mathbb{V}_m$. This is true for a single blob $\tilde{\mathbb{V}} = (3/2) \mathbb{V}$ but it is not trivial in the multiblob due to the effect of \mathbf{P} acting on a spread field made up of significant kernel overlap. For neutrally buoyant multiblobs the added mass consistency implies that $\tilde{\mathbb{V}}_m / \tilde{\mathbb{V}} = \mathbb{V}_m / \mathbb{V}$. It is possible to analytically evaluate the multiblob volume $\mathbb{V}_m^{-1} = (1/N^2) \sum_{i,j} \mathbf{J}_i \mathbf{S}_j$ in the $\mathbf{P} = 1$ case. The overlap integrals are just $\mathbf{J}_i \mathbf{S}_j = \int \delta_h(\mathbf{r} - \mathbf{q}_i) \delta_h(\mathbf{r} - \mathbf{q}_j) d\mathbf{r}$. We have performed such calculation in the continuum setting using $\Phi(x) = (2/3) \cos(2\pi x/3)^2$ (which is extremely close to 3pt Peskin’s function). Theoretical results for $\mathbb{V}_m / \mathbb{V}$ shown in Fig. 2 are in perfect agreement with $\tilde{\mathbb{V}}_m / \tilde{\mathbb{V}}$ obtained from the incompressible solver, indicating that the significant blob-overlaps do not alter the consistency of the added mass effect of the multiblob.

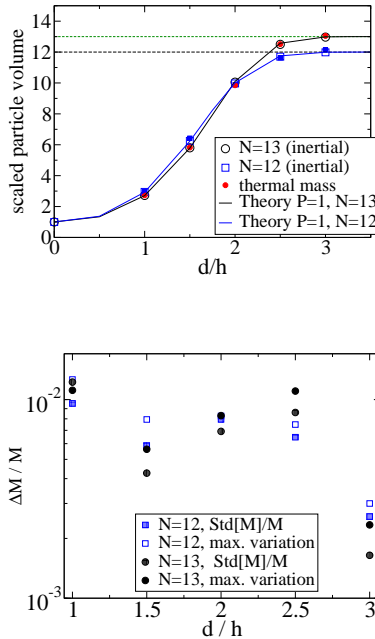


FIG. 2: Top: Volume of the multiblob particle scaled with the isolated blob volume \tilde{V}_m/\tilde{V} versus the neighbor vertex distance d of the icosahedron model. Numerical results were carried out in an incompressible fluid (where the single blob volume is $\tilde{V} = (3/2)V$ due to the added mass effect). Filled symbols corresponds to thermal measurements and empty symbols come from the inertial evaluation of the particle mass $M = \rho_m \tilde{V}_m$ in the neutrally buoyant case ($\rho_m = \rho_f$). Solid line corresponds to the theoretical result of Eq. (47) for the compressible ($P = 1$) case: in this case the mass is scaled with the blob mass $\rho_f V$, with $V = 8h^3$. Relative maximum variation of the particle mass (or volume \tilde{V}_m) over the grid versus the vertex distance d .

Figure 2 presents results for the “filled” $N = 13$ icosahedron and for the icosahedron “shell” with $N = 12$. Numerically, the volume \tilde{V}_m was obtained from the mass of neutrally buoyant particles $\tilde{V}_m = M/\rho_f$ which was evaluated following both inertial and thermal routes. In the thermal route we measured $M_{\text{th}} = k_B T / \langle U_0^2 \rangle$ averaging the squared particle velocity over long simulations where hydrodynamic fluctuations were set in the fluid at finite temperature. We also measured M_{th} from the initial ballistic regime of the mean square displacement of the particle (see below), getting the same outcome. Figure 2 shows the consistency between the inertial and thermal measurements. As shown in the same figure, relative mass variations $\Delta M/M = \Delta \tilde{V}_m/\tilde{V}_m$ are found to be smaller or about than 1% for any vertex separation d considered. It is somewhat surprising that for $d > 1.5h$ relative variations in multiblob volume (or mass) are significantly smaller than that found for a single blob.

2. Moment of inertia and rotation radius

We performed evaluations of the moment of inertia of the multiblob for different d , both from the inertial and thermal routes. Both methods provided perfectly consistent results. The deviation of the moment of inertia over the mesh was found to be quite small, typically about 1% or less. The moment of inertia of the multiblob and its mass can be used to determine a physical radius of the multiblob. The moment of inertia of a solid icosahedron measured with its radius a , equals that of the sphere. In fact, instead of presenting results for \mathcal{I} , we find more practical to present the results for this “radius of inertia” R_I , defined from the relation,

$$\mathcal{I} = \frac{2}{5} M R_I^2 \quad (49)$$

It is important to stress that, like the moment of inertia \mathcal{I} and the mass M , this radius R_I is a “geometrical” property of the multiblob shape and the interpolator S used. This contrasts with the hydrodynamic radius and other measurements of the multiblob size presented below which depends on how the ob-

ject physically perturbs the fluid (which therefore implies finite size effects). Table II presents results for R_I obtained for different icosahedron sizes in the incompressible setting. As stated, \mathcal{I} obtained from equipartition [Eq. (46)] and from the relation between angular acceleration and external torque are in perfect agreement (about 1% deviation). On the other hand, unlike the multiblob scaled volume, the analytic calculation of the moment of inertia from the expression (43) (using $\mathbf{P} = 1$, compressible fluid) reveals that R_I differ in the compressible and the incompressible settings. For small blob overlaps ($d > 3h$) both (compressible and incompressible) values of R_I converge, however as the overlap increases ($d \leq 1.5h$) the solenoidal projection \mathbf{P} of the inner multiblob spread field makes R_I^2 about 2/3 smaller in the incompressible case.

V. MULTIBLOB STOKESLET BEHAVIOR

As a first step in the analysis of the hydrodynamic response of the multiblob model, we analyze its Stokeslet from the hydrodynamic perturbation it creates at long distances from its center. Like in subsequent analyses we will derive effective hydrodynamic radius of the multiblob particle by comparing its behavior with that of a rigid sphere. We will then study the dynamic response of the particle from its mean square displacement and calculate its self-diffusion constant, to cross-check with the friction coefficient via the Einstein relation [36].

A. Hydrodynamic radius

To measure the particle hydrodynamic radius R_H of the multiblob we ascribe the traction exerted by its own perturbative field [12, 26, 37] to the friction a rigid (no-slip) sphere would feel under the same circumstance, $6\pi\eta R_H u_0$. According to the Stokes relation, the friction coefficient $6\pi\eta R_H$ is just the ratio between a (small) pulling force F_0 and the particle translational velocity, U_0 . In a periodic box of size L , the drag increases roughly with L^{-1} due to the interaction of the particle with its own periodic images. This is a real physical effect which corresponds to the increase of drag felt by a particle in a regular array of particles separated by distance L . The analytic solution of this problem (Hasimoto [38]) permits to extrapolate the hydrodynamic radius to infinite boxes $L \rightarrow \infty$, the dominant term in the drag reduction scaling like $1/L$. Assuming that the Stokes relation is valid for a single particle in our periodic box, its drag $F = 6\pi\eta R_H(L)u_0(L)$ is independent on the box size, leading to the following ratio between R_H in two limiting box sizes [12, 26]

$$\frac{R_H(\infty)}{R_H(L)} = 1 - 2.84 \frac{R_H(\infty)}{L} + \mathcal{O}\left(\left(\frac{R_H(\infty)}{L}\right)^3\right); \text{ i.e.,} \quad (50)$$

$$R_H(\infty) = \frac{R_H(L)}{1 + 2.84 \frac{R_H(L)}{L}}, \quad (51)$$

which provides $R_H(\infty)$ from the outcome any finite box L . Unless explicitly stated, we use R_H to indicate $R_H(L \rightarrow \infty)$. Figure 3 shows R_H versus the icosahedron vertex distance d . The first observation is that both models ($N = 12$ blobs in an empty icosahedron and the filled icosahedron with $N = 13$) have quite similar hydrodynamic radius; the $N = 12$ model having a slightly larger R_H at the largest d considered. This indicates that the monopole contribution to the particle disturbance at long distances is essentially controlled by the ‘‘shell’’ of the multiblob and not by its core or inner part. The maximum variation of R_H along the grid (in Fig. 3 bottom) was found to be of the same order than for a single blob, and even smaller for $d > 1.5h$. Thus kernel overlaps in the multiblob are not strongly affecting the grid dependence on R_H . The highest relative variation of R_H over the grid were found for $d = 1h$ (5% variation) and $d = 1.5h$ (2.8%) and $\Delta R_H/R_H$ substantially decreases for $d > 1.5h$ (see Fig. 3).

Figure 3 compares R_H with other relevant sizes of the model: its radius (i.e., the radius of the embedding sphere) $a \simeq 0.95106d$ and the Faxén radius of the average kernel, given by its second moment $\mathcal{J}[(\mathbf{r} - \mathbf{q})^2]^{1/2}$ [see Appendix, Eq. (62)], whose discussion is deferred to Sec. X.

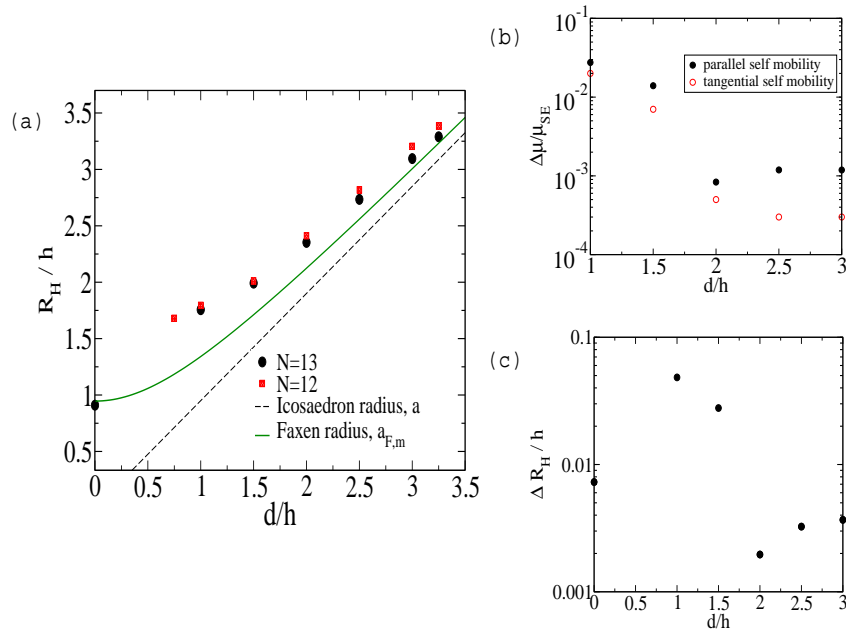


FIG. 3: (a) Hydrodynamic radius in infinite box extrapolated from simulations with $L = 64h$ and $L = 128h$. (b) Relative deviation of the self mobility tensor components from the isotropic case (deviations scaled with the parallel Stokes-Einstein mobility) (c) Maximum variation of R_H over the grid. (b) and (c) corresponds to $N = 13$.

B. Self mobility

Pulling experiments of single particles through the fluid grid also serves to evaluate its self mobility tensor $\boldsymbol{\mu}$ via the relation,

$$\mathbf{U}_0 = \boldsymbol{\mu}\mathbf{F}_0 \quad (52)$$

The velocity of the particle in the pulling direction \mathbf{n} and in the perpendicular direction \mathbf{t} is determined by the components of the mobility $\mu_n = \boldsymbol{\mu} \cdot \mathbf{n}$ and $\mu_t = \boldsymbol{\mu} \cdot \mathbf{t}$. The self mobility tensor of an isotropic particle, with three perpendicular axis of symmetry, is a scalar $\boldsymbol{\mu} = \mu\mathbf{1}$ [6]. Ideally this should be the case of our icosahedron model, with a parallel mobility $\mu_n = \mu_S$ (where $\mu_S = 1/(6\pi\eta R_H)$ is the Stokes mobility) and a vanishing lift term $\mu_t = 0$. The maximum relative deviations $\Delta\mu/\mu_S$ over different grid locations are shown in Fig. 3 for different particle sizes d . Deviations are less than 1% and decrease to about 0.1% for $d > 1.5h$. In the smallest particles ($d = h$) these 1% deviations in tangential mobility around zero (average value over the grid) induces a slight oscillation in the particle translation and a slight “heading” in its motion due to (similarly small) variations in the translational-rotational mobility over the grid (which is also zero for isotropic particles [6]).

C. Mean square displacement

We have analyzed the Brownian motion of the multiblob icosahedron including hydrodynamic fluctuations in a fluid with zero average velocity. The objective is to compare its mean square displacement (MSD) with that of a sphere so as to check the consistency of the model at several scale times. In particular, at small times the ballistic regime depends on the particle mass. At long diffusive times, the self friction ξ and the diffusion coefficient are related $D = kT/\xi$, according to the Einstein relation. At large enough Schmidt number $Sc = \eta/(\rho_f D)$ (typically for $Sc > 20$) the friction coefficient converges to the Stokes value $\xi = 6\pi\eta R_H$, however at small Sc deviations from the Stokes limit occur (see Ref. [36]). We have observed this effect in simulations with $Sc \simeq 10$, however the results presented hereafter correspond to $Sc \simeq 40$ for which the Stokes friction holds with large accuracy [36]. In figure 4 we draw the MSD of two differently sized icosahedrons, $d = h$ and $d = 2.5h$ in a $L = 64h$ box and compare the result

Parameter	Value
Fluid density ρ_f	5.0
Dynamic viscosity η	2.5
Box size L	128.0 or 256.0 for icosahedrons 64.0 for blobs
Cell size h	2.0
Vertexes distance d	Variable, from h to $3.25h$
Interblob spring constant k_{sp}	2×10^4

TABLE I: Common parameters used in all simulations. All particles neutrally buoyant $m_e = 0$

with the theoretical MSD for spheres with the same hydrodynamic radius and mass in an incompressible fluid with the same density and viscosity. The theoretical MSD is calculated from the friction memory function derived by Bedeaux and Mazur in [39]. Both cases agree quite well with the theory for spheres over all time scales. In particular, the particle (thermal) mass determined by the slope of the ballistic regime equals that obtained by other means (equipartition and inertial methods) and at longer times, the diffusion constant is consistent with the observed friction (Einstein relation). Slight deviations at times smaller than the viscous time t_ν are visible for the $d = h$. These come out from the coupling of the high frequencies of the elastic structure and the translational motion of the multiblob. Such coupling is not a numerical artifact, but rather a physical effect which has been recently theoretically studied by Felderhof [28]. The effect is clearly observed in the velocity autocorrelation function (VAF) shown in Fig. 5 and consists on a jitter of the translational velocity of the elastic structures moving in incompressible fluid. Consistent with the ratio between the spring time $t_{sp} = (\rho_f \tilde{V}/k_{sp})^{1/2}$ and the momentum diffusion time $t_\nu = R_H^2/\nu$ (we used $t_\nu/t_{sp} \simeq 80$), the amplitude of such oscillations start at about $0.01 t_\nu$ and decay (probably exponentially [28]) in time. Although we have not yet studied this in detail, we observe that the jitter is drastically reduced if the particle size is increased (see Fig. 5 for $d = 2, 5 h$). This is consistent with the analysis presented in Ref. [28] and also with the decrease in the non-dimensional group $(kT/k_{sp}a^2)^{1/2}$ introduced before. Contrary to the prediction of Ref. [28] we do not observe the suppression of the added mass effect in the VAF of the elastic structure, whose value at $t = 0$ is still reduced by a factor $2/3$ (see Ref. [24, 25]). Note that in the blob model the particle is “filled” with fluid and thus conserves its volume, which is not true for the theoretical framework [28]. A study of this effect should probably require working in the compressible formulation.

VI. ROTLET AND ROTATIONAL DIFFUSION

The angular friction on a rotating sphere $8\pi\eta R^3$ and the sphere rotational diffusion are also related by the Einstein formula, $D_r = k_B T/(8\pi\eta R^3)$. We have evaluated the rotational diffusion D_r of multiblobs with different sizes from the time integral of the autocorrelation of the multiblob angular velocity. As for the hydrodynamic radius in relation with the Stokeslet, we can evaluate an effective multiblob radius associated to its rotlet, i.e. to its inertialess rotation dynamics. This is just, $R_r \equiv [k_B T/(8\pi\eta D_r)]^{1/3}$. The effect of the particle rotation on the fluid propagates like $1/r^3$ so finite size effects are less relevant than in the Stokeslet case. As shown in Table II, for any d , the “rotlet” radius R_r is consistent with R_I and R_H , with a particularly good agreement in the range $1.5 \leq d/h \leq 2.5$.

Figure 5(bottom) shows the time autocorrelation of the angular velocity and compares our numerical results for $d = 2h$ with the theoretical curve derived in Ref. [40] for a sphere of radius R_I . The time-axis is scaled with the rotational relaxation time $\tau_r = 1/(6D_r)$ and the y-axis with $3k_B T/I_{sp}$ with $I_{sp} = (8/15)\pi\rho R_I^5$. This scaling permits to observe deviations from the sphere behaviour in different regimes. In particular, deviations are expected at small times ($t < 0.01\tau_r$) because of the difference in the inertial masses (the mass of sphere $4\pi\rho R^3/3$, differs from the multiblob mass in Fig. 2). Interestingly, as the momentum diffusion takes over, both (theoretical and numerical) curves overlap quite exactly and converge to the limiting $t^{-5/2}$ power law. The excellent agreement found in diffusive regimes using R_I as the scaling radius explains the slight difference between R_I and R_r ; as the later is obtained from the whole integral of $\langle \Omega(t)\Omega(0) \rangle$, which also includes the transition (inertial-to-diffusive) regime into account.

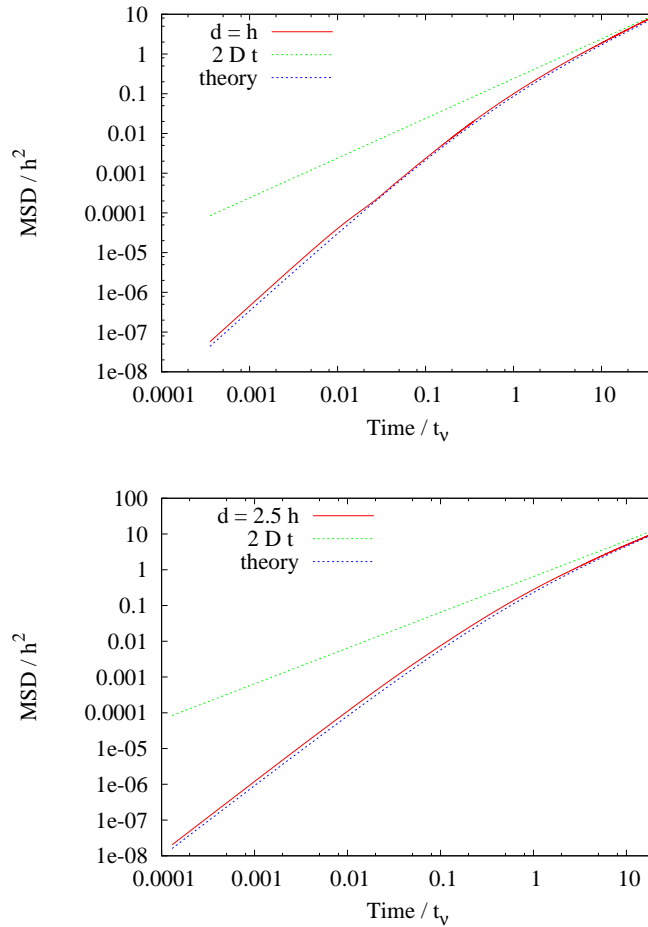


FIG. 4: Mean square displacement of multiblob icosahedrons compared with the analytic result for a sphere with the same hydrodynamic radius. Results correspond to the filled icosahedron $N = 13$ in $L = 64h$ boxes and other data in Table I. The fluid temperature is $k_B T = 3$ and Schmidt number $Sc = 40$. The diffusion constant D comes from the Einstein relation, $D = k_B T / (6\pi\eta R_H)$.

VII. VELOCITY PROFILES

Over the following sections we focus on the hydrodynamics at close distances from the particle center $r \sim R_H$. We start with the fluid velocity profile past a multiblob particle moving at constant velocity U_0 in a fluid which would be otherwise at rest.

A. Empty and filled model comparison

Figure 6 compares the velocity profile past the $N = 12$ empty icosahedron and the filled one with $N = 13$ blobs. The result for the single blob is added for reference. In these test the ratio $L/R_H(L)$ is approximately fixed to have similar finite size contributions. The first feature to highlight in Fig. 6, is that the empty multiblob $N = 12$ suffers from substantial fluid leakage inside its body kernel. In this sense its behavior resembles the single blob case. By contrast, the extra blob placed at the icosahedron center ($N = 13$ multiblob) avoids the fluid leakage and furnishes a particle with an impenetrable core where the relative particle-fluid velocity is zero. The filled icosahedron multiblob, with $N = 13$, seems therefore better suited to simulate suspensions of rigid impermeable colloids and in the remainder of this section we focus on the near-field behavior of the $N = 13$ model.

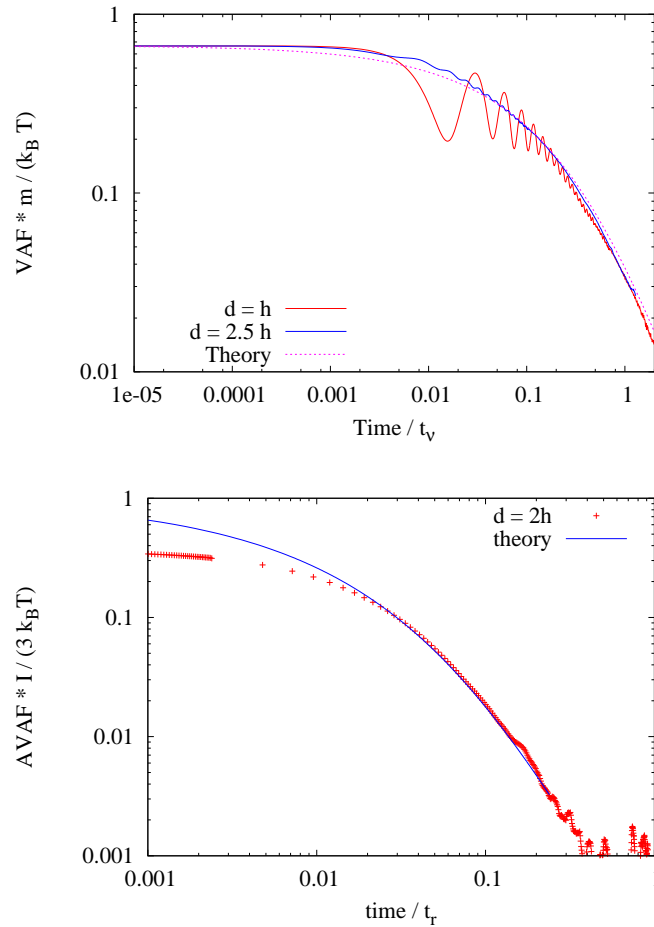


FIG. 5: Top panel: Velocity autocorrelation function for the MSD curves of Fig. 4. Time is scaled with $t_v = R_H(L)^2/\nu$ and the theoretical result corresponds to a sphere with radius similar to the hydrodynamic radius of the icosahedron in an incompressible fluid. Bottom panel shows the time autocorrelation of the angular velocity $\langle \Omega(t)\Omega(0) \rangle$ for $d = 2h$ and compare it with the theoretical result for a sphere [40] of radius R_I . The time axis is scaled with the rotation relaxation time $\tau_r = 8\pi\eta R_I^3/(6k_B T)$ and the y-axis with the sphere $\langle \Omega^2 \rangle$ covariance: $3k_B T/I_{sp}$ with $I_{sp} = 2/5 M_{sp} R_I^2$ and $M_{sp} = (4/3)\pi\rho_p R_I^3$. All cases correspond to neutrally buoyant particles, $\rho_p = \rho_f$.

B. Filled multiblob and sphere

In the following sections the hydrodynamic behavior of the multiblob particle is analyzed by comparison with sphere results. The sphere is used here as the reference model, in part due to the wealth of theoretical (and experimental) results it offers. The fluid velocity past multiblob particles (in the zero Reynolds regime) is compared in Fig. 7 with the analytic solution for a rigid sphere with no-slip boundaries. The best fit to the sphere provides an estimation of the location of its effective *no-slip surface*, related to the its hydrodynamic size *at close distances*. Due to the intermediate level resolution of our model, which does not explicitly resolves the body surface (but rather its “hydrodynamic” volume) this effective no-slip radius R_s differs from the hydrodynamic radius R_H obtained from its response as a monopole (Stokeslet) at long distances. Differences in these long and short range radius estimations are not large and decrease with the particle size. These are analyzed in Sec. X but before that, we will show that mutual mobilities, lubrication and stresslet arising from higher multipole contributions in the near-field are consistent with the same effective “no-slip” sphere radius.

Figure 7 shows the velocity profiles around the multiblob icosahedron. These figures correspond to averages over many different orientations of the icosahedrons. Comparisons are made with the flow past a rigid no-slip sphere with radius R_s (dashed lines), whose radial v_r and tangential v_θ components vary

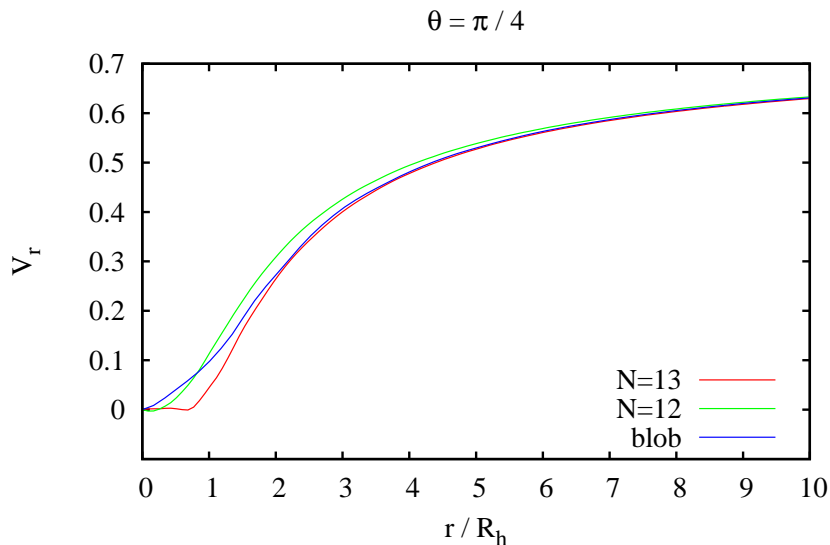


FIG. 6: Radial component of the velocity profile along the direction forming $\theta = 45^\circ$ with the direction of the constant plug velocity field. Results corresponds to the zero Reynolds limit for a blob particle ($R_H(L) = 1.86h$ in a $L = 64h$ box), and a multiblob particle with $N = 12$ (hydrodynamic radius $R_H(L) = 1.83h$) and $N = 13$ (filled icosahedron with $R_H(L) = 1.83h$) in both cases with $d = h$ and boxes of $L = 128h$.

with the distance to the particle center r as,

$$\frac{v_r}{u_0 \cos \theta} = 1 - \frac{3 R_s}{2 r} \left[1 - \frac{1}{3} \left(\frac{R_s}{r} \right)^2 \right] \quad (53)$$

$$\frac{v_\theta}{u_0 \sin \theta} = 1 - \frac{3 R_s}{4 r} \left[1 + \frac{1}{3} \left(\frac{R_s}{r} \right)^2 \right] \quad (54)$$

Here \mathbf{r} is the radial vector with origin in the particle center and θ is the angle between the particle velocity \mathbf{U}_0 and \mathbf{r} . Figure 7 shows reasonably good fits to the sphere velocity profiles of Eq. (53). The effective radius of the sphere R_s which best fits the multiblob velocity profiles at close distance is indicated in the figure legend. The value of R_s of the multiblob icosahedron model provides an estimation of its “no-slip” radius, compatible with a rigid sphere. The fitting procedure involves adjusting several curves with one only parameter (R_s) whose fitting uncertainty is about $0.05h$.

We note that in these fits (see Fig. 7) we only consider the velocity profile near the particle, at distances of about $r < 2R_s$ where higher moments (less sensitive to the effect of periodic images) become important. We observed that the box size L does not affect the estimation of R_s more than the inherent uncertainty of the method. As a final comment, we find remarkable the extremely small fluid leakage observed in the largest particles considered (see Fig. 7), whose vertex distances reach up to $3.25h$ and correspond to non-overlapping blob kernels (the blob kernel width is $3h$). This is probably due to the good behavior of Peskin’s kernels and opens the possibility of studying polydispersity effects with the very same model, over a range of particle radius up to about 3.5 times larger than the blob.

VIII. MUTUAL FRICTION AND LUBRICATION FORCES

The mutual friction induced by hydrodynamic coupling between two particles is now analyzed. More precisely, by pulling two particles with equal by opposite sign forces and measuring the resulting linear and angular particle velocities, we obtain the pair mobility dependence with their distance. The impact parameter (closest distance between linear trajectories) was set to zero in a series of simulations dedicated to lubrication forces while, in another set the impact parameter was chosen to be about the hydrodynamic

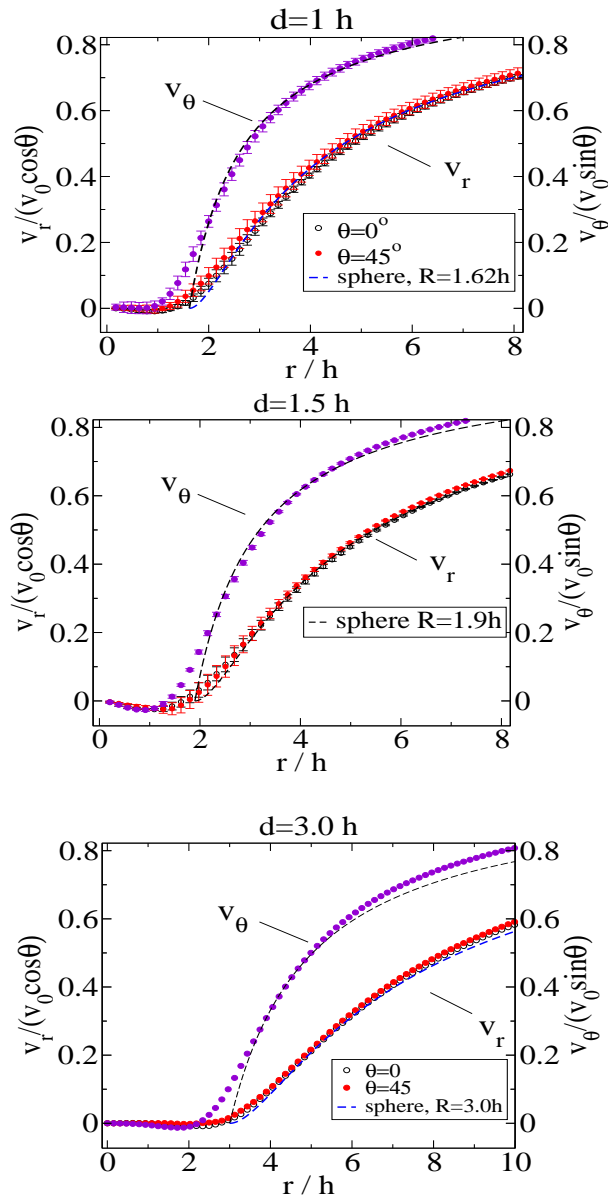


FIG. 7: Normal and tangential components of the velocity profiles past a multiblob particle (filled icosahedrons with $N = 13$) moving at constant velocity in the zero Reynolds limit. Results correspond to several values of the vertex distance d . Dashed lines indicate the velocity profile of a rigid sphere with an effective “no-slip” radius R_s , specified for each case. All cases corresponds to $L = 128h$ (with $h = 2$).

diameter. In this second set of simulations particles pass-by at close distance which permit to measure the tangential component of the mutual mobility and the induced translation-rotation coupling.

A. Normal, tangential friction and rotational coupling

Here we present results for a set of simulations where two particles approach each other and pass by at close distance. Both particles are pulled by similar forces in opposite directions $\mathbf{F}_1 = \mathbf{F} = -\mathbf{F}_2$.

The setup, sketched in Fig. 8, corresponds to a finite impact parameter of about the particle diameter (nearly touching spheres). To compare the results of the multiblob particles with rigid spheres we use the theoretical result obtained from the method of multiple reflections (four reflections) valid up to $O(r^{-6})$ [1]

$$6\pi\eta R_s \mathbf{U}_0^{(1)} = \mathbf{F} \cdot [A(r)\mathbf{e}_r\mathbf{e}_r + B(r)(\mathbf{1} - \mathbf{e}_r\mathbf{e}_r)] \quad (55)$$

$$6\pi\eta R_s^2 \boldsymbol{\Omega}^{(1)} = \mathbf{F} \times \mathbf{e}_r \frac{3}{4} \left(\frac{R_s}{r}\right)^2 \quad (56)$$

here \mathbf{r} is the vector joining the two particle centers $\mathbf{r} = \mathbf{r}_2 - \mathbf{r}_1$ and $\mathbf{e}_r = \mathbf{r}/r$. The angular velocity of sphere 1 is $\boldsymbol{\Omega}^{(1)}$ and equals $-\boldsymbol{\Omega}^{(2)}$. The functions $A(r)$ and $B(r)$ determine the amplitude of the normal and tangential frictions, respectively along \mathbf{e}_r direction and the perpendicular direction coplanar to \mathbf{F} . These functions are,

$$A(r) = 1 - \frac{3}{3} \left(\frac{R_s}{r}\right) + \left(\frac{R_s}{r}\right)^3 - \frac{15}{4} \left(\frac{R_s}{r}\right)^4 \quad (57)$$

$$B(r) = 1 - \frac{3}{4} \frac{R_s}{r} - \frac{1}{2} \left(\frac{R_s}{r}\right)^3 \quad (58)$$

Figure 8 shows $\tilde{A} \equiv 6\pi\eta \mathbf{U}_{0,\parallel}/F_{\parallel}$ and $\tilde{B} \equiv 6\pi\eta \mathbf{U}_{0,\perp}/F_{\perp}$ with $F_{\parallel} = \mathbf{F} \cdot \mathbf{e}_r$ and $F_{\perp} = |\mathbf{F} - \mathbf{F} \cdot \mathbf{e}_r \mathbf{e}_r|$. A perfect agreement with the result for sphere of radius R_s would correspond to $\tilde{A} \rightarrow A(r)/R_s$ and $\tilde{B} \rightarrow B(r)/R_s$. As shown in the figure, for $d = h$, the value $R_s \simeq 1.65h$ provides a reasonable good fit with the multiblob icosahedron. The best correspondence for the $d = 1.5h$ case is found to be for $R_s \simeq 1.90h$. These values are within 3% with those observed in the velocity profiles. Also to check for finite box effect we reproduced some of the cases with different box sizes. Fig. 8 shows a comparison for the mobility functions $A(r)$ and $B(r)$ in the $d = 1.5h$ case obtained with boxes of $L = 64h$ and $128h$. The agreement of both curves for $r < 10h$ is perfect, showing no trace of finite box size effects. These effects start to be visible for $r > 10h$ which corresponds to about $r > 5R_s$.

When a particle pass by near by another a torque is induced by hydrodynamic coupling. In terms of mobilities, two particles of radius R moving nearby at distance r by a constant force \mathbf{F} experience an rotation whose angular velocity (up to $O(R/r)^6$) is given by Eq. (56). To this order in the inverse particles distance, multiple reflections theory [1] indicates that the ratio between the angular rotation $\boldsymbol{\Omega}$ and the induced torque $\mathbf{F} \times \mathbf{e}_r$ is independent on the particle radius (note that R_s^2 appears in both sides of Eq. 56). Thus, comparison with the multiple reflection solution to $O(r^{-6})$ serves as a check of the model consistency at moderate distances, but does not bring about any estimation of the particle “effective radius”. Figure 9 compares both signals in the case of our multiblob model for $d = 1.5h$. In these tests, the forces \mathbf{F} were in x -direction and the angular velocity was perpendicular to the $\mathbf{F} - \mathbf{r}$ plane. The other two components of $\boldsymbol{\Omega}$ oscillate around zero. For $r > 1.5R_s$ results agree with Eq. (56) while at shorter distances the angular velocity substantially increase. According to numerical results (see Fig. 9) the next term in the expansion of Eq. (57) could be $2(R_s/r)^6$ (with $R_s = 1.9h$). In any case, the increase in angular velocity at close distances is qualitatively consistent with the weak divergence of the angular velocity at short distances predicted by the lubrication theory.

B. Lubrication

Figure 10 presents the results of two particles approaching each other with zero impact parameter. As stated, we pulled both particles with a constant force in opposite directions (i.e. the total momentum added to the flow is zero) and calculate the particles velocities. This is a mobility calculation, although in Fig. 10 we present the results in terms of friction (inverse of the mobility), by scaling the applied force F with the velocity of one of the particles.

The top pannel of Fig.10 presents the scaled friction force F/F_{Stokes} (with $F_{Stokes} = 6\pi\eta R_H(L)u_0^{(1)}$) against the scaled distance $r/R_H(L)$. This scaling permits to compare with the single blob behavior [24, 26], whose mobility is compatible with Rotne-Prager-Yamawaka [41]. Results for multiblobs merge with the Rotne-Prager result for $r > 2.5R_H$. However at shorter distances a large increase of friction is observed, which seems to diverge at finite interparticle distance. This nice multiblob “divergent

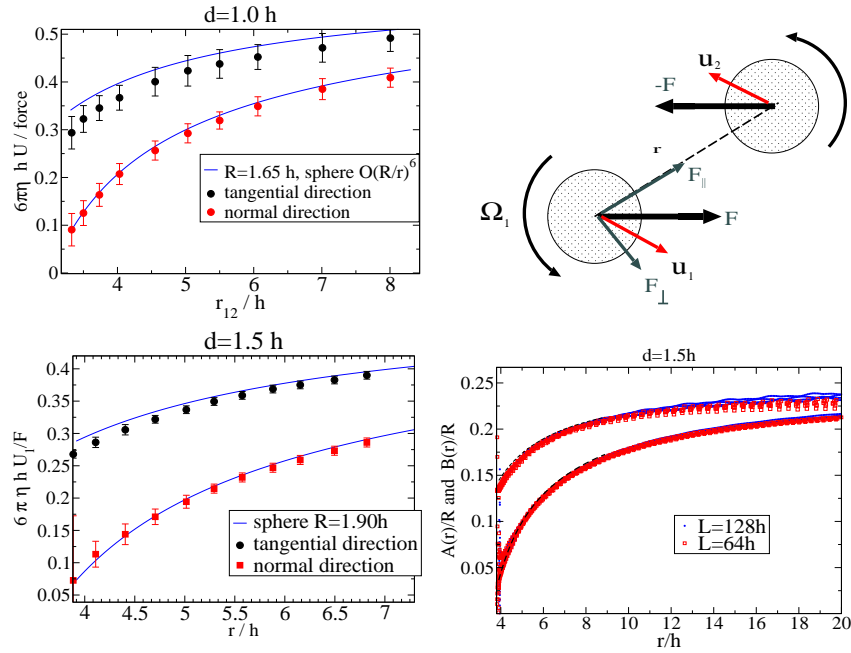


FIG. 8: Mutual friction between two particles approaching at non-zero impact parameter as specified in the sketch. In each panel, the upper curves are obtained from the tangential mobilities and the lower ones from normal mobilities. The tangential component of any vector (e.g. pulling force) being $\mathbf{F}_\perp \cdot (\mathbf{1} - \mathbf{e}\mathbf{e})$ and the normal one $\mathbf{F}_\parallel \cdot \mathbf{e}\mathbf{e}$, where $\mathbf{e} = \mathbf{r}_{12}/r_{12}$. The dashed curves are fits to the multiple reflection expansion for two spheres (errors of order $O(R/r)^6$) in Eq. 57 using values of sphere effective radius R indicated in the legends. The size of the box in the left panels is $L = 64h$. In the right panel (bottom) we compare results for $d = 1.5h$ in two boxes $L = 128h$ and $L = 64h$.

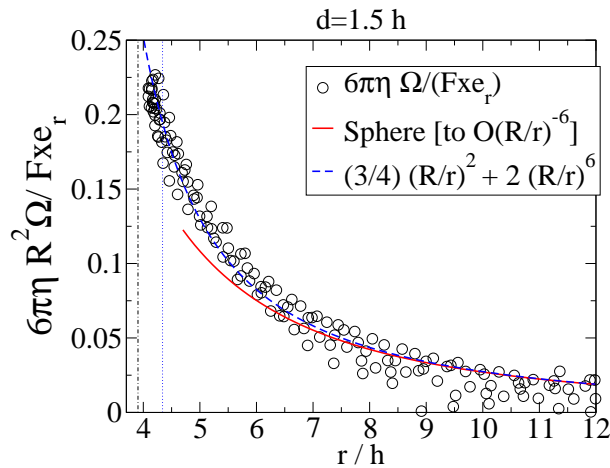


FIG. 9: The ratio $6\pi\eta R^2 \Omega / |\mathbf{F} \times \mathbf{e}_r|$ where Ω is the angular velocity of one sphere induced by hydrodynamic interaction with another sphere passing close-by (see the sketch of the setup in Fig. 8). Solid lines corresponds to the sphere result (third reflection) $(3/4)(R/r)^2$, which is valid up to $O(r^{-6})$. The dashed line adds the next term in the expansion obtained by a fit to numerical results for which we have used the mobility effective radius $R = R_s = 1.9h$.

lubrication” stems out from the single blob mutual friction, which (see Fig. 10) is known also to “diverge” once two blob kernels fully overlap [26]. As expected, the multiblob divergence is however not fully compatible with a rigid sphere. This is shown in Fig. 10 by including Brenner’s analytic solution for two approaching spheres [42] (see also Ref. [43]). Using an effective sphere radius of $0.85 R_H(L)$ the agreement with a rigid sphere holds up to distances of about $1.85 R_H(L)$, where friction forces are about 6 times larger than the Stokes drag.

It is noted that in using the term *divergent lubrication* for the multiblob we are abusing the terminology as, strictly speaking, we have not identified a coordinate (e.g. distance between closest blobs) which unambiguously determines the location of the divergence (see Fig. 10). In terms of grid mesh units, the “divergence” of multiblob friction was observed to occur within a range of distances $(2.6 \pm 0.2)h$ which is roughly independent on the icosahedron size d . This is shown in the bottom panel of Fig. 10 which presents the ratio $F/(6\pi\eta hU_0)$ (converging to $R_H(L)/h$ at large interparticle separations r). The objective of Fig. 10 (bottom) is to compare the lubrication of the multiblobs with that of two spheres having the effective “no-slip” radius R_s derived in previous sections (from velocity profiles and mobilities, see Figs. 8 and 7). The agreement is excellent up to $r > 2.2R_s$ indicating the consistency with near-field hydrodynamics. However, due to a “softer” hydrodynamic interaction, the “divergence” of multiblob friction takes place at distances somewhat shorter than $2R_s$. In the next section we show how to benefit from the “natural” lubrication of the model to recover the viscosity of dense colloidal suspensions.

All cases of Fig. 10 corresponds to the “filled” $N = 13$ multiblob. However, it is interesting to note that calculations performed with the $N = 12$ icosahedron “shell” reported the same outcome for the mutual friction, meaning that the large increase in lubrication between two multiblobs is essentially determined by the external blobs and not by the inner blob.

IX. STRESSLET AND VISCOSITY

This section analyzes an extremely important property of rigid particles, which is their ability of exerting a finite stress in the fluid. In particular, rigid particles cannot deform and impose a constraint on the local fluid velocity gradients, which vanish inside the particle domain. This requires a work done by the particle cohesion forces, which appears as an extra virial term in the fluid stress tensor coming from the fluid-particle interaction [1]. This virial contribution, derived in Eq. (35) for the present model, increases the fluid stress and also the effective viscosity of the colloidal solution, which is nothing but the ratio between the stress and the fluid overall deformation rate. For the reasons explained in Sec. III C the contribution of particle shape fluctuations in the viscosity are vanishingly small and they behaves like rigid spheres.

The viscosity of a colloidal solution is a long standing problem which have been studied by many authors [44]. The problem is usually posed in the low Reynolds limit $\text{Re} = \rho_f VR/\eta \ll 1$, and this leaves at least two controlling parameters: the volume fraction of the colloids ϕ and the Peclet number $\text{Pe} = VR/D$, with $D = k_B T/(6\pi\eta R)$ the colloid diffusion coefficient. The fluid environmental velocity V depends on the type of flow considered, here, we have used a protocol to measure the viscous contribution of the particles in the limits $\text{Pe} = 0$ and Schmidt number $\text{Sc} = \eta/(\rho D) \rightarrow \infty$.

The viscosity was measured using a standard non-equilibrium procedure; i.e., by exerting a periodic density force to the fluid ($\mathbf{f}(\mathbf{r}, t) = f_0 \sin(k_j y)\hat{\mathbf{x}}$) and measuring the response of the velocity field in the x direction. The viscosity is the ratio

$$\eta = \frac{f_0}{k_j^2 v_x}, \quad (59)$$

where v_x is the amplitude of the sinusoidal x -velocity profile formed along the y direction. The wavenumber is $k_j = 2j\pi/L$ with j a natural number so that the wavelength $\lambda = L/j$ fits in the periodic box of side L .

In calculating the stress contribution from the particles one needs to sample all possible particle configurations in the fluid which in a straightforward simulation would imply letting the particles diffuse over the system and explore their configurational and positional phase space. Indeed, due to the large time separation between the spring dynamics and the particle diffusion dynamics, this straight procedure is far from efficient, specially in the limit $\text{Pe} \ll 1$. Instead, we decided to adopt a sort of mixed Monte Carlo approach.

Initially, random configuration on non-overlapping particles were generated for a given concentration ϕ and box size L using the Monte Carlo method. No shear was introduced during this part of the process and therefore the Peclet number was strictly zero. In this preparatory step, the particle interaction potential was chosen to be the hard-sphere potential so as to avoid any influence of the shape of continuous (soft) repulsive cores on the calculation. The radius of the hard-sphere interaction is noted as R_{HS} and it is indeed a free parameter, such as any other set of possible interparticle interaction parameters (depletion, electrostatic, etc.) would be. We chose a collection of independent configurations compatible

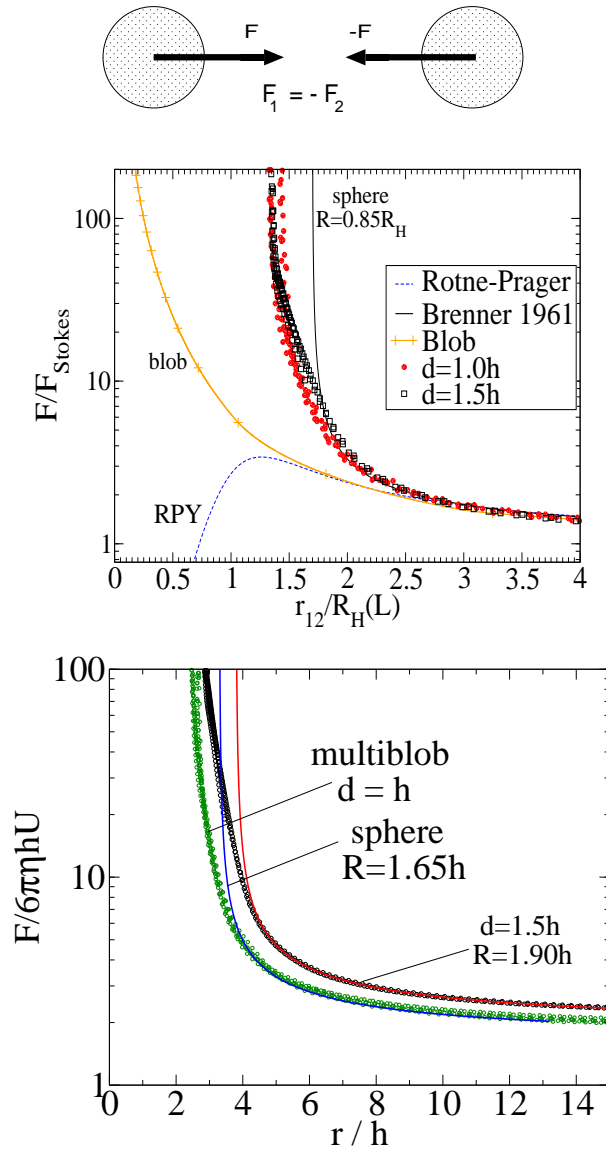


FIG. 10: Drag force on one particle due to the mutual friction with another one approaching in frontal collision (zero impact parameter). Both particles being pulled with the same force F in opposite directions (see the sketch). Top panel: friction force scaled with the Stokes force against the scaled distance $r/R_H(L)$. At large distances $r > 2.3R_H$ the single blob and multiblob scaled friction coincide with the Rotne-Prager-Yamawaka analytic approximation. For $r > 1.85R_H$, the multiblob friction agrees with Brenner's [42] analytic solution of two approaching spheres (we use an effective sphere radius $0.85R_H(L) \simeq R_s$). Bottom panel: the mutual multiblob friction scaled with $6\pi\eta hU_0^{(1)}$ is compared with Brenner's analytic result for two rigid spheres [42] with effective no-slip radii R_s , indicated in the legend. All multiblob simulations with $L = 128h$ and $N = 13$.

with the hard-sphere potential and the thermodynamic state, and for every configuration we ran a short simulation in the presence of shear so as to measure the effect of the extra stress on the system on the amplitude of the velocity profile. To avoid a long relaxation time coming from the fluid inertia, for this second set of *hydrodynamic* simulations we used the Fluctuating Immersed Boundary method for Brownian hydrodynamics that we have recently derived [33]. This algorithm works in the limit $Sc \rightarrow \infty$ in which the relaxation of the fluid momentum is instantaneous. However, we let the initial configuration relax over a small set of iterations to allow the particles springs to adapt to the flow strain: the system is relaxed over 4000 time steps and the velocity profile averaged over 100 time steps ($\Delta t = 10^{-3}$).

This method proved to be quite efficient for the present purposes. In particular it permits to surpass the bottleneck of the long diffusive sampling times, which are dominant at $Pe \rightarrow 0$ (the situation is not

that critical as $Pe > 1$). In this study particles do not interact via potential forces, however, the same idea could be in principle extended to interacting particles, provided the particle configurations are sampled from a Monte Carlo code and sequentially fed to the hydrodynamic solver. This is so because, physically, the positional and configurational probability distributions does not depends on the hydrodynamics in the regime of low Peclet numbers.

Results for η presented below are robust against changes in the wavelengths λ of the external force, which we varied to check that the measured viscosity corresponds to the $\lambda \rightarrow \infty$ (macroscopic) limit (see Fig. 11). The viscosity of molecular liquids is known to depend on the wavenumber and $\eta(k) \rightarrow \eta(0)$ for $kR \simeq 1$ [45]. Although this effect in colloidal hydrodynamics is potentially interesting by itself, here λ was chosen much larger than the colloidal size to avoid observing any dependence of η with the perturbative flow wavelength. Also, we varied L for fixed λ to test any possible finite size effect due to the box periodicity. The results for $\eta(\phi)$ in Fig. 11), are quite satisfactory in these respects, showing that finite size effects are absent (either in λ or L).

1. Dilute and semidilute regime

Values of the colloidal solution viscosity $\eta(\phi)$ obtained for the $d = h$ icosahedron are reported in Fig. 11. The viscosity increases with the particle volume fraction $\phi = (4/3)\pi R_{\text{HS}}^3 n L^{-3}$ with n the number of particles in the system. Using $R_{\text{HS}} = 1.62 h$ we recover an excellent agreement with the classical Einstein relation

$$\eta = \eta_0 \left(1 + \frac{5}{2} \phi \right), \quad (60)$$

which is valid at very low dilutions, as can be also seen in Fig. 11. At higher concentration of colloids, the viscosity has also contributions from the hydrodynamic coupling between particles [1, 46] which induce a quadratic term in the virial expansion of η . The result, originally derived by Batchelor [46] is

$$\eta = \eta_0 \left(1 + \frac{5}{2} \phi + 6.2 \phi^2 + \dots \right). \quad (61)$$

The quadratic regime in the viscosity solutions of colloidal spheres is also shown in Fig. 11. Quite importantly, the theoretical sphere trend is recovered for $R_{\text{HS}} = 1.62 h$, which is in excellent agreement with values of R_s obtained from velocity profiles and mutual friction $R_s = (1.63 \pm 0.03) h$.

2. Dense regime

As shown in Fig.11, for $\phi > 0.2$ the viscosity obtained for multiblobs with hard-spheres of radii $R_{\text{HS}} = R_s = 1.62 h$ is somewhat below the sphere trend reported by Brady and Sierou [10]. This was to be expected because although multibody hydrodynamic interactions are taken into account, the lubrication curve for our multiblob model peaks off (or “diverges”) at interparticle distances smaller than $2 R_s$. In other words, for $R_{\text{HS}} = 1.62 h$ the large lubrication regime of the model is screened by the particles excluded volume. However, to deal with the dense regime one can slightly modify the hard-sphere interaction so as to allow the model unfold the required amount of lubrication. In particular, to resolve the large lubrication regime we tried multiblobs with hard-sphere radius $R_{\text{HS}} = 1.55 h$ (instead of $1.62 h$). Results, shown in Fig. 11 are in very good agreement with rigid spheres up to $\phi \simeq 0.45$. We believe this is an outstanding result as it naturally stems from the fluid solver, and does not requires ad hoc lubrication corrections [7, 17]. At this highly concentrated solutions, the hydrodynamic interaction is essentially short-ranged, so the mismatch between the potential interaction radius $1.55 h$ and the hydrodynamic radius of one isolated particle is not really important for the physics involved. We have not tried to further increase the particle volume fraction towards 0.5 (in fact, the preparation of the initial configuration becomes really hard); however to resolve the lubrication of this extremely dense regime we could still further reduce the excluded volume radius to about $R_{\text{HS}} \simeq 1.50 h$.

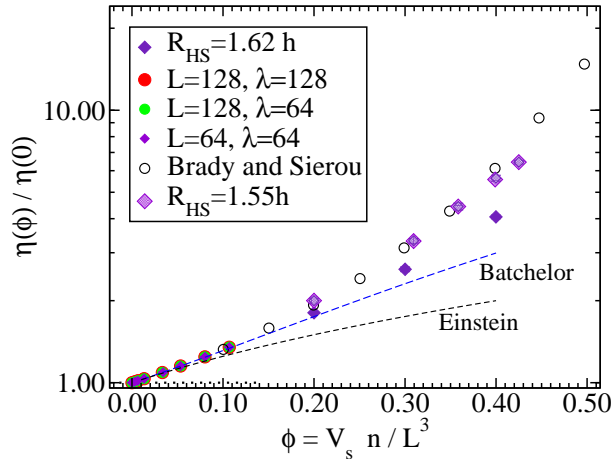


FIG. 11: Intrinsic viscosity of a dispersion of multiblob particles at increasing volume fraction ϕ . Simulations correspond to $d = h$ in periodic boxes of different length, imposing a sinusoidal $\sin(2\pi y/\lambda)$ shear stress acting over x direction. The best fit to the Einstein linear regime $\eta(\phi) = \eta_0 (1 + 2.5\phi)$ at low volume fraction ϕ provides the effective particle volume $\mathcal{V}_s = (4\pi/3) R_s^3$ compatible with the sphere behavior. The effective particle radius resulting in $R_s = 1.62h$. At larger $\phi < 0.15$ we find excellent agreement with the Batchelor regime. For denser suspensions we compare the results obtained for hard-spheres of radii R_{HS} , with the fully resolved simulations result of Brady and Sierou [10]. Multiblobs with $R_{HS} = 1.55h$ are in very good agreement up to $\phi \simeq 0.45$.

X. CONSISTENCY IN THE PARTICLE HYDRODYNAMIC SIZE

Contrary to other models in this field [7, 18, 20–22], our multiblob design is not based on resolving the particle surface, but rather its core, and this necessarily implies some uncertainty its hydrodynamic size. This section compares the results for filled icosahedrons multiblobs of different sizes (vertex distances between $d = h$ and $d = 3.25h$) and fixed number of blobs ($N = 13$).

TABLE II: Radii of the multiblob icosahedrons of vertex distance d obtained from different routes. Second column; radius of inertia R_I evaluated by fitting the moment of inertia of the multiblob icosahedron to a sphere $R_I = ((5/2)\mathcal{I}/M)^{1/2}$. The mass M is obtained from Eq. 47. Errors bars in R_I are around $0.01h$. Third column: hydrodynamic radius $R_H(L \rightarrow \infty)$ obtained from the Stokeslet response. Fourth column: rotlet radius R_r from rotational diffusion (see Sec. IV C 2). Fifth column: the *no-slip* radius obtained from best fits of the sphere colloids near-flow perturbation, mutual mobility, lubrication and Stresslet. All quantities in unit of the Eulerian grid mesh h .

d	R_I	R_H	R_r	R_s
0 (blob)	-	0.91	-	-
1.0	1.61	1.76	1.50	1.62 ± 0.03
1.5	1.85	1.99	1.90	1.87 ± 0.03
2.0	2.18	2.35	2.36	2.30
2.5	2.67	2.73	2.63	2.70
3.0	3.30	3.08	3.30	3.00 ± 0.05

To begin with, the radius of inertia of the particle R_I calculated in Sec. IV C 2, is just a property of the particle shape (more properly, of the distribution of the forming blobs) and of the interpolators used (here 3 pt Peskin kernels). R_I can be sought as a reference particle size, which should ideally be consistent with the disturbances created by a multiblob in the fluid.

The hydrodynamic response of the multiblob essentially depends on the relative importance of the multipole terms of the perturbative flow. The multiblob monopole is relevant at long distances and was made compatible with the Stokeslet of a rigid no-slip sphere of radius R_H . Following the standard procedure [12], we call R_H the multiblob hydrodynamic radius, which depends on the box size L due to well established finite size effect in periodic space. As shown in Table II, we found that for $d < 3h$, the hydrodynamic radius $R_H(L \rightarrow \infty)$ is slightly larger than R_I .

Hydrodynamic properties, such as the the fluid velocity profiles past a fixed multiblob and the mutual friction are much less sensitive to finite size effects, reflecting the relevance of the near-field response dictated by higher order terms of the multipolar expansion. In all these tests we found that the multiblob behavior is consistent with an effective sphere of radius R_s . Lacking a better name, we called R_s the effective *no-slip* radius and found that the validity of this “short-range” regime extends up to distances of about $r \sim 5 R_s$ away from the particle center (see Figure 10). Consistently with this observation, the stresslet in the dilute regime was also found to be compatible with rigid no-slip spheres of radius R_s . The same applies for the rotational friction R_r which we found in relative good agreement with R_s .

Figure 12 illustrates the flow streamlines past a multiblob particle, and compares it with the single blob case. The hydrodynamic radius R_H and the no-slip radius R_s have been indicated with lines. The iso-values of the fluid velocity in x direction, clearly indicates that at $r \simeq R_s$ the gradient of the stream-function in normal direction vanishes, meaning zero fluid-particle relative velocity. This outlines the particle “core”, as shown in Fig. 12. By contrast the blob model lacks a core domain in proper sense. In Fig. 12 we have chosen a relative large particle $d = 3h$ in a small box $L = 64h$ to illustrate the case with the largest difference in $R_H(L) \simeq 3.5h$ and $R_s \simeq 3.0h$. This difference ($0.5h$ in the example) decreases with L as $R_H(\infty) < R_H(L)$ but *also* with the particle size a . To understand the overall trend of the model’s radii it is illustrative to derive the so-called Faxén radius of the multiblob kernel, $a_{F,m}$. We get (see Appendix),

$$a_{F,m}^2 = \mathcal{J} \left[(\mathbf{r} - \mathbf{q}_0)^2 \right] = a_F^2 + a^2. \quad (62)$$

were we recall that $a = 0.9511 d$ is the embedding sphere radius of the icosahedron and, similarly, a_F^2 is the Faxén square radius of the blob kernel (i.e. its second moment) [24, 33] given by,

$$a_F^2 \equiv 3 \int \delta(\mathbf{r}) r_\alpha^2 d\mathbf{r}^3 = \mathbf{J} [\mathbf{r}^2]. \quad (63)$$

Its value (for the 3pt kernel) is $a_F \simeq (0.95 \pm 0.05) h$, quite close to the blob Stokeslet radius $R_H = 0.91 h$ [24, 33].

The relation (62) indicates that the relative difference $(a_{F,m} - a)/a$ decreases with the geometric radius a , scaling like a^{-2} . Such scaling corresponds to the ratio between the volume of the blob kernel shell $4\pi a^2 a_F$ and the total particle volume $4(\pi/3)a^3$. Thus the deviations found in the effective radii decrease quadratically with the multiblob size a , as highlights Fig. 13. The result of Eq. (62) together with Figs. 3 and 13 suggest ways to reduce the uncertainty in size: for instance using higher order kernels for the blobs in shell of the particle to reduce a_F and sharpen the body surface to get $a \simeq a_{F,m} \simeq R_H \simeq R_s$. This however, might spoil the good lubrication properties of this model, although it is something to be explored in future works.

We conclude this section with some general comments on what is the best choice for the value of d . The first issue to indicate is that the size of the simulation box has to be $L \propto R_H$ while the computational cost (fluid cells) scales at least like L^3 . Thus small particles (i.e. small values of d) reduce simulation costs. To give one example, the smallest particles used in Refs. [17, 19, 21] are about $R = 8h$, while using $d = h$ ($R_H \simeq 1.6h$) we reduce the number of fluid cells embedding the colloids in about $(8/1.6)^3 = 125$ times. Another benefit of small multiblobs is that their lubrication is better resolved due to the shorter difference between their hydrodynamic size and the interparticle distance where the mutual friction diverges (which as stated, was observed to be roughly independent on d). Values of d between h and $1.5h$ provide similar good outcomes in this respect (see Fig.10). Unfortunately, for $d < h$ substantial kernel overlap increases the grid dependence of the particle properties (mass, R_H , R_I).

Finally, an important issue to be considered is the consistency in the particle size, in response to different hydrodynamic interactions (translation, rotation, mutual friction, etc.). In this respect, the main result of the present study is summarized in Table II. It is noted that R_I is only relevant for inertial effects related to rotation, so at small particle Reynolds number, and in the dilute or moderately dense colloidal solutions, the range $1.5 \leq d/h \leq 2.5$ provides a save choice with differences in radii of less than about 5%. The value $d = 2.5h$ provides a particularly consistent set of radii (also with R_I) as can be seen in Table II.

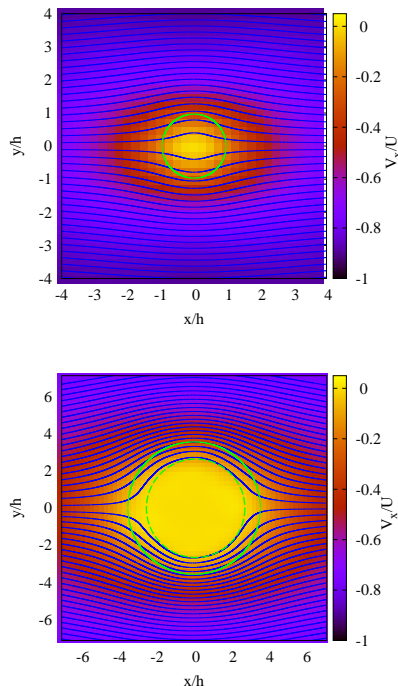


FIG. 12: The streamlines around a fixed single blob (top) facing a plug flow, compared with those created by a filled icosahedron formed by $N = 13$ blobs (one in its center) and inter-vertex distance $d = 3h$. The Reynolds number is very small so the flow is symmetric in the fore and aft-directions. Colours indicate isovalues of the flow velocity in the direction of the particle motion (x). The solid green circle around the multiblob particle indicates the location of its hydrodynamic radius $R_H(L)$ (with $L = 64h$ in the figure) and the dashed circle the location where the fluid relative velocity approximately vanishes (“effective no-slip radius, R_S ”).

XI. CONCLUSIONS

The present multiblob model targets an intermediate resolution of colloidal particles, using a few overlapping blob kernels (here 12 or 13) to construct relatively small particles. Using an icosahedron as template we get particles radius between $1.6h$ and $3.25h$, with hydrodynamic response compatible with spherical colloids (with or without inertia), in terms of translation and rotation and their couplings, flow perturbation, mutual friction and lubrication forces. The hydrodynamic radius determined from the Stokeslet [see Eq. (50)] is known to depend on the system size L due to periodic images. However, hydrodynamic interactions at short distances are much less sensitive to finite size effects (see e.g. Fig. 8), and the effective particle sizes related to rotation, near-flow perturbative flow and short distance mobilities agree within about 5% for any L .

In the method presented in this paper the hydrodynamic interactions emerge naturally from the fluid solver and the fluid-particle coupling. Notably, our schemes do not need to include ad hoc pair-wise friction patches to model lubrication. The strength of the lubrication force between two multiblobs can be calibrated by slightly modifying their hard-core (or hard-sphere) radius R_{HC} (more precisely the ratio R_{HC}/h which is a free non-hydrodynamic parameter). In particular, we have explored the case of colloidal spheres and were able to reproduce the increase in viscosity up to large volume fractions $\phi \leq 0.45$. In future work this idea will be extended to lubrication in colloids with complex shapes, where theoretical lubrication relations are difficult to implement or even absent. On the other hand, the method allows for an easy and efficient implementation in systems with periodic boundary conditions, for which the incompressibility constraint can be applied with Fast Fourier Transform methods [24]. In the viscosity measurements of Sec. IX our implementation of these schemes for Graphical Processing Units [47] is able to run at about 100 time steps per second for a system of 1000 icosahedron at a volume fraction of $\phi \approx 0.3$ in one standard GPU card (1.4GB); this is about 40 times faster than reported simulations using Accelerated Stokesian Dynamics in a 16 CPU core cluster [48]. This increased efficiency is important to allow for larger temporal windows of observation, necessary to study some non-equilibrium processes

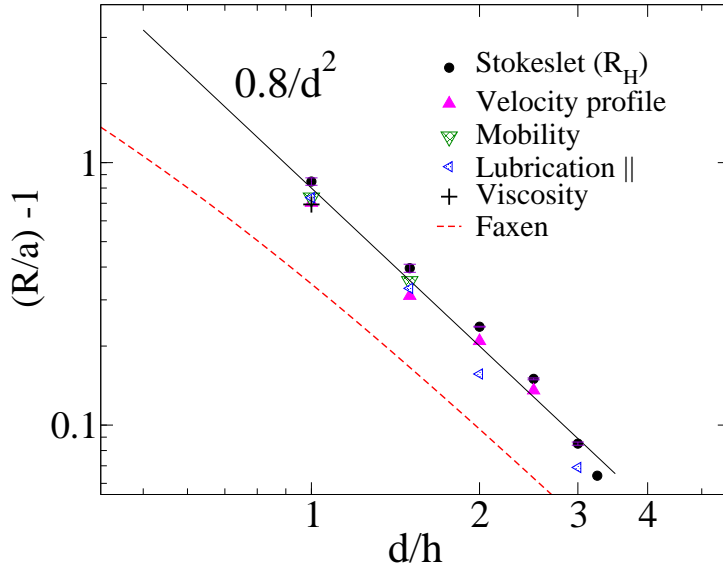


FIG. 13: Relative difference between the effective particle radius estimated by comparison with the sphere behavior under different physical mechanisms R and the geometric radius of the multiblob icosahedron particle.

such as clustering gelation [49–51].

Acknowledgments

We thank Aleks Donev for a critic reading of the manuscript and suggestions. We acknowledge funding from the Spanish government FIS2010-22047-C05, from the Comunidad de Madrid MODELICO-CM (S2009/ESP-1691), Acknowledgment is made to the Donors of the American Chemical Society Petroleum Research Fund for partial support of this research.

Appendix A: Multiblob Faxén radius

We showed in previous works for single blob particles [24, 25] that there is a close relation between the second moment of the kernel and its Faxén radius. We shall show that in the Faxén radius of the multiblob is given by the second moment of the average kernel \mathcal{J} . For a general body shape it consists on a dyadic, which can be directly calculated from the definitions in Eqs. (5), (6) and (7), and using the zeroth and linear consistency of the 3pt Peskin’s (blob) kernel,

$$\mathcal{J} \left[(\mathbf{r} - \mathbf{q}_0)^\alpha (\mathbf{r} - \mathbf{q}_0)^\beta \right] = \frac{a_F^2}{3} \delta_{\alpha,\beta} + \frac{1}{N} \sum_i s_i^\alpha s_i^\beta \quad (\text{A1})$$

Note that the second term in (A1) is just the gyration tensor of the structure. For a platonic solid, such as our icosahedron, $\sum_i s_i^\alpha s_i^\beta = (a^2/3) \delta_{\alpha,\beta}$ where a is the radius of the sphere passing through the vertexes (for our icosahedron $a = \sqrt{(10 + 2\sqrt{5})}/4 d = 0.9511 d$). In this case, the second moment tensor reduces to a scalar times the identity matrix, its trace being

$$\mathcal{J} \left[(\mathbf{r} - \mathbf{q}_0)^2 \right] = a_F^2 + a^2. \quad (\text{A2})$$

where a_F^2 is the second moment of the single blob defined in Eq. (63). The result of Eq. (A2) is interesting because it indicates that the average kernel size (given by its second moment) and the geometric particle size a converge as the particle size is increased, with *fixed number of blobs*.

The Faxén law for particle translation [1, 5] can be used to relate the trajectory of a force-free, inertialess particle in any flow field. To relate the Faxén law with the kernel properties we proceed like

in Refs. [24, 29, 33]: we Taylor expand the flow field $\mathbf{v}(\mathbf{r})$ around the particle center \mathbf{q}_0 and interpolate it on the particle site to obtain $\mathbf{U}_0 = \mathcal{J}[\mathbf{v}(\mathbf{r})]$. One gets,

$$v^\alpha(\mathbf{r}) = v^\alpha(\mathbf{q}_0) + \partial_\beta v^\alpha(\mathbf{q}_0) (r - q_0)^\beta + \frac{1}{2} \partial_\beta \partial_\gamma v^\alpha(\mathbf{q}_0) (r - q_0)^\beta (r - q_0)^\gamma + \dots \quad (\text{A3})$$

Applying the interpolation \mathcal{J} and using the result of Eqs. (A1) and (A2),

$$\mathbf{U}_0 = \mathcal{J}[\mathbf{v}(\mathbf{r})] = \mathbf{v}(\mathbf{q}_0) + \frac{a_F^2 + a^2}{6} \nabla^2 \mathbf{v}(\mathbf{q}_0) + \dots \quad (\text{A4})$$

This result exactly corresponds to the Faxén law [5] on a force-free, inertialess particle of radius $a_{F,m} = (a_F^2 + a^2)^{1/2}$ moving in the fluid field $\mathbf{v}(\mathbf{r})$. Any curvature in the velocity field (here proportional to the local total pressure gradient $\nabla^2 \mathbf{v} = (1/\eta) \nabla p$) induces a departure from the local fluid velocity proportional to the size of the particle. This observation, initially made for the single blob case [24, 33] led us to relate the second moment of the kernel to its ‘‘Faxén radius’’. We also observed that small kernels with non-zero second moment are paradoxically better suited to represent small particles of finite size (for the 3pt kernel $a_F \simeq (0.95 \pm 0.05) h$, which is close to its Stokeslet radius $R_H = 0.91 h$).

In passing we note that for non-isotropic particles, Eq. (A1) into (A3) shows that departures of the particle trajectory from the unperturbed fluid trajectory are proportional to the contraction of the triadic $\nabla \nabla \mathbf{v}(\mathbf{q}_0)$ with the gyration tensor of the structure $(1/N) \sum_i \mathbf{s}_i \mathbf{s}_i$.

-
- [1] S. Kim and S. Karrila, *Microhydrodynamics: Principles and Selected Applications* (Butterworth Heinemann, Boston, 1991).
 - [2] H. Lowen, *Journal of Physics: Condensed Matter* **24** (2012).
 - [3] J. K. Eaton, *International Journal of Multiphase Flow* **35**, 792 (2009), ISSN 03019322, URL <http://linkinghub.elsevier.com/retrieve/pii/S0301932209000330>.
 - [4] A. T. Cate, J. J. Derksen, L. M. Portela, and H. E. A. V. den Akker, *J. Fluid Mech.* **519**, 233 (2004).
 - [5] J. K. G. Dhont, *An Introduction to Dynamics of Colloids*, vol. 2 of *Studies in Interface Science* (Elsevier, 1996), studies in ed., ISBN 9780444820099.
 - [6] H. Happel and J. Brenner, *Low Reynolds number hydrodynamics with special applications to particulate media* (Martinus Nijhoff Publishers, The Hague, 1983).
 - [7] F. Janoschek, J. Harting, and F. Toschi, arXiv preprint arXiv:1308.6482 (2013).
 - [8] K. Amit, *TESIS* (Chicago, 2009).
 - [9] G. M. Cicuta, E. Onofri, M. C. Lagomarsino, and P. Cicuta, *Phys. Rev. E* **85**, 016203 (2012), URL <http://link.aps.org/doi/10.1103/PhysRevE.85.016203>.
 - [10] A. Sierou and J. F. Brady, *J. Fluid Mech.* **448**, 115 (2001).
 - [11] G. Muldowney and J. J. L. Higdon, *Journal of Fluid Mechanics* **298**, 167–192 (1995).
 - [12] B. Dünweg and A. J. C. Ladd, *Advances in Polymer Science* **221**, 89 (2009).
 - [13] Y. T. Chew, C. Shu, and Y. Peng, *Journal of Statistical Physics* **107** (2002).
 - [14] L. Ferrás, J. Nóbrega, and F. Pinho, *International Journal for Numerical Methods in Fluids* **72**, 724 (2013), ISSN 1097-0363, URL <http://dx.doi.org/10.1002/flid.3765>.
 - [15] R. Kapral, *Advances in Chemical Physics* **140**, 89 (2008).
 - [16] M. Bian, Xin; Ellero, *Computer Physics Communications* **185**, 53 (2014).
 - [17] N.-Q. Nguyen and A. Ladd, *Physical Review E* **66**, 046708 (2002), ISSN 1063-651X, URL <http://link.aps.org/doi/10.1103/PhysRevE.66.046708>.
 - [18] M. Uhlmann, *Journal of Computational Physics* **209**, 448 (2005).
 - [19] W.-P. Breugem, ASME 2010 3rd Joint US-European Fluids Engineering Summer Meeting and 8th International Conference on Nanochannels, Microchannels, and Minichannels FEDSM-ICNMM2010 (2010).
 - [20] Z.-G. Feng and E. E. Michaelides, *Journal of Computational Physics* **202**, 20 (2005), ISSN 00219991, URL <http://linkinghub.elsevier.com/retrieve/pii/S0021999104002669>.
 - [21] J. Molina and R. Yamamoto, *J Chem Phys.* **139**, 234105 (2013).
 - [22] C. Peskin, *Acta Numerica* **11**, 479 (2002), URL http://journals.cambridge.org/abstract_S0962492902000077.
 - [23] P. J. Atzberger, P. R. Kramer, and C. S. Peskin, *Journal of Computational Physics* **224**, 1255 (2007).
 - [24] F. Balboa Usabiaga, R. Delgado-Buscalioni, B. E. Griffith, and A. Donev, *Computer Methods in Applied Mechanics and Engineering* **269**, 139 (2014).
 - [25] F. Balboa Usabiaga, *Minimal models for finite particles in fluctuating hydrodynamics* (Universidad Autonoma de Madrid, Madrid, 2014).
 - [26] F. Balboa Usabiaga, I. Pagonabarraga, and R. Delgado-Buscalioni, *Journal of Computational Physics* **235**, 701 (2012), ISSN 00219991, URL <http://linkinghub.elsevier.com/retrieve/pii/S0021999112006493>.

- [27] A. P. S. Bhalla, R. Bale, B. E. Griffith, and N. A. Patankar, *Journal of Computational Physics* **250**, 446 (2013), ISSN 0021-9991, URL <http://www.sciencedirect.com/science/article/pii/S0021999113003173>.
- [28] B. U. Felderhof, *Physical Review E* **89** (2014).
- [29] F. Balboa Usabiaga and R. Delgado-Buscalioni, *Physical Review E* **88** (2013).
- [30] A. M. Roma, C. S. Peskin, and M. J. Berger, *J. Comput. Phys.* **153**, 509 (1999).
- [31] R. Zwanzig and M. Bixon, *Journal of Fluid Mechanics* **69**, 21 (1975).
- [32] L. D. Landau and E. M. Lifshitz, *Fluid Mechanics* (Pergamon Press, New York, 1959).
- [33] S. Delong, F. Balboa Usabiaga, R. Delgado-Buscalioni, B. E. Griffith, and A. Donev, *Journal of Chemical Physics* **140**, 134110 (2014).
- [34] In particular, $\mathbb{I}_c = \sum_{i,j} \mathbf{s}_i \cdot \mathbf{s}_j [\mathbf{1Tr} - \mathbf{1}] \mathbf{J}_i \mathbf{P} \mathbf{S}_j - \mathbf{J}_i \mathbf{P} \mathbf{S}_j : \mathbf{s}_i \mathbf{s}_j \mathbf{1} - \text{Tr}(\mathbf{J}_i \mathbf{P} \mathbf{S}_j) \mathbf{s}_i \mathbf{s}_j + \mathbf{J}_i \mathbf{P} \mathbf{S}_j \cdot \mathbf{s}_i \mathbf{s}_j + \mathbf{s}_i \mathbf{s}_j \cdot \mathbf{J}_i \mathbf{P} \mathbf{S}_j$, where $\text{Tr} \mathbf{A} = A^{\alpha, \alpha}$ is the trace operator.
- [35] A. Pinelli, I. Naqavi, U. Piomelli, and J. Favier, *Journal of Computational Physics* **229**, 9073 (2010), ISSN 00219991, URL <http://linkinghub.elsevier.com/retrieve/pii/S0021999110004687>.
- [36] F. Balboa Usabiaga, X. Xie, R. Delgado-Buscalioni, and A. Donev, *Journal of Chemical Physics* **139**, 214113 (2013).
- [37] M. R. Maxey and J. J. Riley, *Physics of Fluids* **26**, 883 (1983).
- [38] H. Hasimoto, *J. Fluid Mech.* **5**, 317 (1959).
- [39] P. Mazur and D. Bedeaux, *Physica* **76**, 235 (1974).
- [40] A. V. Zlatovskiy, *Izv. Vuzov. Fizika* **10** (1969).
- [41] J. Rotne and S. Prager, *Journal of Chemical Physics* **50**, 4831 (1969).
- [42] H. Brenner, *Chem. Engng. Sci.* **16**, 242 (1961).
- [43] R. E. Hansford, *Matematika* **17**, 270 (1970).
- [44] N. J. Wagner and J. F. Brady, *Physics Today* **October**, 27 (2009).
- [45] J. P. Hansen and I. R. McDonald, *Theory of Simple Liquids* (Academic Press, New York, 1986).
- [46] G. K. Batchelor, *An Introduction to Fluid Dynamics* (Cambridge University Press, Cambridge, 1967).
- [47] F. Balboa Usabiaga, *fluam*, available at <https://code.google.com/p/fluam/>.
- [48] K. Yeo and M. R. Maxey, *Journal of Computational Physics* **229**, 2401 (2010).
- [49] A. de Candia, E. D. Gado, A. Fierro, and A. Coniglio, *Journal of Statistical Mechanics: Theory and Experiment* p. P02052 (2009).
- [50] J. K. Whitmer and E. Luijten, *The Journal of Physical Chemistry B* **115**, 7294 (2011).
- [51] X. Cao, H. Cummins, and J. Morris, *Journal of colloid and interface science* **368**, 86 (2012).